High-pressure synthesis and physical properties of perovskite and post-perovskite Ca_{1-x}Sr_{x}IrO_{3}

J.-G. Cheng, J.-S. Zhou, J. B. Goodenough, Y. Sui, Y. Ren, and M. R. Suchomel

Phys. Rev. B **83**, 064401 — Published 9 February 2011
DOI: 10.1103/PhysRevB.83.064401

High-pressure synthesis and physical properties of perovskite and post-perovskite $Ca_{1-x}Sr_xIrO_3$

J.-G. Cheng[1,2], J.-S. Zhou[1*], J.B. Goodenough[1], Y. Sui[2], Y. Ren[3], and M. R. Suchomel[3]

[1] Texas Materials Institute, University of Texas at Austin, Austin, TX 78712, USA

[2] Center for Condensed Matter Science and Technology, Department of Physics,

Harbin Institute of Technology, Harbin, 150001, China

[3]Advanced Photon Source, Argonne National Laboratory, Argonne, Illinois 60439, USA

Abstract

The post-perovskite (pPv) is the high-pressure phase of some highly distorted perovskites. The pPv phase of $MgSiO_3$ stabilized under 125 GPa and 2000 K cannot be quenched to ambient pressure. In contrast, the pPv $CaIrO_3$ can be synthesized under a modest pressure or even at ambient pressure. However, the pPv $CaIrO_3$ has not been fully characterized. We report here systematic structural studies, measurements of transport and magnetic properties including critical phenomena, specific heat, and thermal conductivity in a series of samples $Ca_{1-x}Sr_xIrO_3$ synthesized under high pressure. The $Ca_{1-x}Sr_xIrO_3$ samples exhibit an evolution from the pPv phase to the perovskite phase. We have also prepared the perovskite (Pv phase) $CaIrO_3$ with the wet chemical method. Rietveld refinements of the pPv and Pv phase $CaIrO_3$ have been made based on high-resolution synchrotron diffraction. In comparison with effects of the chemical substitution on the crystal structure and physical properties, we have studied the structure and magnetic properties of the pPv $CaIrO_3$ under hydrostatic pressure. Results have been discussed in the context of orbital ordering biased by the intrinsic structural distortion and the strong spin-orbit coupling that is much enhanced in these 5d oxides with the pPv structure.

PACS numbers: 71.70.Ej, 75.30.Et, 75.40.Cx, 75.30.Cr, 72.20.Pa

Introduction

Transition-metal oxides with perovskite or perovskite-related structure offer a variety of physical properties due to an interplay of electron–electron/spin–spin and electron–lattice interactions; these properties include the high-T_c superconductivity in copper oxides, magnetoresistance in manganese oxides, and multiferroic phenomena. Most of these studies have been carried out on 3d transition-metal oxides. In the 4d and 5d transition-metal oxides, however, competition from the spin-orbit (SO) coupling becomes important on top of the interplay mentioned above. The orbital angular momentum of an atomic state is quenched or significantly reduced in a solid where the eigenfunctions in the crystal field are real. In 3d perovskites, intrinsic structural distortions [1,2] bias long-range, cooperative orbital ordering that suppresses the orbital angular momentum, and the spin-orbit coupling is negligible. In contrast, orbital degeneracy survives so as to preserve the orbital moment in some 4d and 5d oxides. The iridate oxides [3] [4] [5] [6] [7] [8] [9] [10] [11] [12] [13] [14] are good candidates to show the competition between electron-lattice, spin-orbit, and spin-spin interactions since the SO coupling parameter λ increases with atomic number Z for d electrons of a given column of the periodic table.[15] A new Mott insulator with $J_{\mathrm{eff}}=1/2$ in which the total spin is coupled with the orbital moment L=1 from *t* orbitals, has been indeed confirmed in the layered perovskite Sr_2IrO_4 (K_2NiF_4 structure) by photoemission [16] and resonant x-ray scattering. [17] In comparison, isostructural Sr_2RhO_4 is metallic,[18] and its SO coupling is relatively weak. The addition of the SO coupling to the spin-spin interaction creates a complicated paramagnetic susceptibility that either does not follow a Curie-Weiss law at all or fitting to a CW law gives an unphysical Weiss constant and effective moment. To resolve the Hamiltonian in which the intraatomic SO coupling and the interatomic spin-spin interaction have equal footing is an interesting theoretical challenge [19].

Most irridates studied so far are with the K_2NiF_4 structure. The symmetry of the tetragonal K_2NiF_4 structure includes a four-fold rotation axis along the *c* axis, which allows degenerate $zx \pm iyz$ orbitals at an octahedral-site transition-metal cation. Therefore, a low-spin Rh(IV): $4t^5e^0$ or Ir(IV):$5t^5e^0$ cation in this structure with an $(xy)^2\ (zx \pm iyz)^3$ configuration retains an orbital angular momentum. A local octahedral-site distortion to two short *c*-axis bonds and four long basal-plane bonds would signal the presence of this orbital order and therefore also of a strong SO coupling at a localized-electron manifold.

Instead of corner-shared octahedra in perovskite or perovskite related structures, octahedra are connected by sharing edges in the layered pPv structure. The local octahedral-site distortion, i.e. two short and four long bonds, in the pPv $CaIrO_3$ is consistent with the $(xy)^2\ (zx \pm iyz\ )^3$ type orbital ordering. The pPv $CaIrO_3$ phase has received significant attention from geologists in recent years since it has the same structure as the unquenchable pPv phase of $MgSiO_3$ obtained under $P > 125$ GPa and $T \approx 2000$ K [20]. Discovery of the phase transition to the pPv structure in $MgSiO_3$ and the follow-up studies provide good opportunities to understand Earth's lowest mantle (the so-called D'' layer) [20, 21]. Most of these studies on pPv $CaIrO_3$, however, have been limited to the structure under high pressure and high temperature [22] [23] [24] [25] [26] [27] [28], which meet the major interests of geologists. Although why the highly dense perovskite structure becomes unstable against the pPv structure under high pressure is not yet clear, the transition seems always to occur under a sufficiently high pressure in the highly distorted perovskites. This conclusion is supported by successful high-pressure syntheses of new pPv phases $CaMO_3$ (M = Ru, Rh, and Pt) [29] [30] [31] [32] [33] that are all quenchable to ambient pressure. The diamagnetic pPv $CaPtO_3$ with low-spin Pt(IV) $5t^6e^0$ allows us to extract the intrinsic structural distortion without interference from the feedback effect of orbital-lattice interaction.

Ohgushi and his co-workers [34] [35] [36] have investigated the transport and magnetic properties of the pPv $CaIrO_3$ and the Na doped $Ca_{1-x}Na_xIrO_3$ at cryogenic temperatures. The pPv $CaIrO_3$ is a weak-ferromagnet insulator with $T_c \approx 115$ K. Na doping induces an insulator-metal transition. In this paper, we report physical properties of the system $Ca_{1-x}Sr_xIrO_3$ ($0 \leq x \leq 1.0$) synthesized under high pressure. The pPv phase has been found within $x < 0.3$, whereas the Pv phase dominates in the Sr-rich compositions.

Experimental details

Polycrystalline pPv $Ca_{1-x}Sr_xIrO_3$ ($0 \leq x \leq 1.0$) samples were prepared in a Walker-type multianvil pressure module. First, stoichiometric mixtures of $CaCO_3$, $SrCO_3$ and Ir metal powders were thoroughly ground and sintered in air at 900°C and 950°C for 24 h each. The resultant precursors, which contain a mixture of Ca_2IrO_4, perovskite phase, and IrO_2, were subjected to a high-pressure and high-temperature (HPHT) treatment under 4GPa and 1150°C for 30 min. Details about the HPHT experiments can be found elsewhere [37]. The perovskite (Pv) phase of $CaIrO_3$ used in this study was synthesized by thermal decomposition of the hydroxide intermediate $CaIr(OH)_6$ at 600°C for 10h in air.[38] We have made $CaIr(OH)_6$ in the following reaction scheme:[38]

$K_2IrCl_6 \xrightarrow{H_2O} IrCl_6^{2-} \xrightarrow{KOH,\, pH\, 7-8} Ir(OH)_6^{2-} \xrightarrow{Ca^{2+}} CaIr(OH)_6\downarrow$. We found that the pH value of 10-12 given in the paper [38] will result in more Ca_2IrO_4 impurity in the final product. Decomposition of the $CaIr(OH)_6$ at 600°C for more than 10 h or at higher temperatures produces a mixture of Pv and pPv phases. The phase purity of the obtained samples was examined with powder X-ray diffraction (XRD) at room temperature with a Philips X'pert diffractometer (Cu Kα radiation). In order to obtain more reliable structural parameters of pPv and Pv phases of $CaIrO_3$, high resolution synchrotron powder diffraction data were collected at room temperature using beamline 11-BM (λ = 0.41221Å) [39] at the Advanced Photon Source (APS), Argonne National Laboratory. The obtained XRD profiles were analyzed by the Rietveld method with the FULLPROF program.[40] The DC magnetization and specific heat were measured with a commercial Superconducting Quantum Interference Device (SQUID) magnetometer and a Physical Property Measurement System (PPMS) (Quantum Design), respectively. The magnetic susceptibility under high pressure was measured with a miniature Cu-Be cell fitting the SQUID magnetometer. A piece of Pb as the pressure manometer, the sample, and a mixture of 3M Flourinert FC77 + FC 72 as the pressure medium were sealed in a Teflon capsule. The steady-state method was used in the thermal conductivity measurement. The thermoelectric power was measured with a home-made setup. A four-probe method was used to measure the resistivity.

Results and Discussion

I. Crystal structures and their influence on the orbital moment in the pPv and Pv phases of $CaIrO_3$

Depending on the synthesis procedure, $CaIrO_3$ can be made with two different orthorhombic polymorphs, [41] the *Pbnm* perovskite (Pv) phase with $a \approx 5.346$ Å, $b \approx 5.587$ Å and $c \approx 7.672$ Å and the *Cmcm* pPv phase with $a \approx 3.145$ Å, $b \approx 9.857$ Å and $c \approx 7.296$ Å. Although the reversible Pv to pPv phase transition can be seen by *in-situ* X-ray diffraction of $MgSiO_3$ under high pressure and temperature [20], this transition has not been observed for the Pv $CaIrO_3$ under up to 30 GPa of hydrostatic pressure.[22] [42] The Pv $CaIrO_3$ in Fig.1(a) is built up from corner-shared $IrO_{6/2}$ octahedra in three dimensions with large Ca cations in the interstitial positions. The pPv phase $CaIrO_3$ [43] in Fig.1(b), has a layered structure. Patterns of high-resolution XRD and results of Rietveld refinements with the structural models in Fig.1 are shown in Fig.2 for both the Pv and pPv phases of $CaIrO_3$. Lattice parameters, atomic positions and important bond lengths and bond angles from refinements are listed in Tables 1, 2 and 3. Atomic positions for the pPv $CaIrO_3$ are consistent with those reported in the literature [43]. Rietveld refinement of the Pv $CaIrO_3$ has not been reported in the literature. Octahedral-site distortions can be generally described by the orthorhombic vibrational modes $Q_2 = \ell_x - \ell_y$ and $Q_3 = (2\ell_z - \ell_x - \ell_y)/\sqrt{3}$, where ℓ_x, ℓ_y, ℓ_z are the bond lengths for bonding along x, y, z directions. For the Pv phase, the octahedral-site distortion corresponds to a combination of the Q_2 and Q_3 modes. Octahedra in a [010] layer of the pPv phase form edge-shared rows that are connected to one another by sharing the corner oxygen O_1. The Ir-O_1-Ir bond angle $\theta = 134.48$ ° in this buckled plane is far smaller than the averaged Ir-O-Ir bond angle $\theta = 145.5°$ seen in the Pv phase. The symmetry allows 2×(Ir-O_1) bonds and 4 ×(Ir-O_2) bonds in the pPv structure, whereas there are three different Ir-O bonds, i.e. 2×(Ir-O_1), 2×(Ir-O_{21}) and 2×(Ir-O_{22}) in the Pv structure with the space group *Pbnm*. These different local bonding configurations influence the orbital angular momentum. To help this discussion, we have shown the wave functions in the cubic crystal field in terms of spherical harmonics $\Psi_{\ell,\ell z}$ in Eq.1. A reduced orbital angular momentum $l_z = 1$ is seen in a degenerate $zx \pm iyz$ orbital.

$$\begin{cases} |xy\rangle = \frac{i}{\sqrt{2}}\left(\psi_{2,-2}-\psi_{2,+2}\right) \\ |zx\rangle = \frac{1}{\sqrt{2}}\left(\psi_{2,-1}+\psi_{2,+1}\right) \\ |yz\rangle = \frac{i}{\sqrt{2}}\left(\psi_{2,-1}-\psi_{2,+1}\right) \\ |x^2-y^2\rangle = \frac{1}{\sqrt{2}}\left(\psi_{2,-2}+\psi_{2,+2}\right) \\ |3z^2-r^2\rangle = \psi_{2,0} \end{cases} \qquad \begin{aligned} |\ell_z = \pm 1\rangle &= \frac{1}{\sqrt{2}}\left(|zx\rangle \pm i|yz\rangle\right) \\ &= \frac{1}{\sqrt{2}}\left[\frac{1}{\sqrt{2}}\left(\psi_{2,-1}+\psi_{2,+1}\right) \pm \frac{-1}{\sqrt{2}}\left(\psi_{2,-1}-\psi_{2,+1}\right)\right] \\ &= \begin{cases} \psi_{2,+1} \\ \psi_{2,-1} \end{cases} \end{aligned} \tag{1}$$

In the pPv phase, the octahedral-site distortion corresponds to a negative Q_3 mode (the z axis for a given octahedron is along the Ir-O_1 bond, not the same as that used for the unit cell). As illustrated in the schematic energy diagram before considering the effect of the spin-orbit coupling in Fig.3, the local distortion with a negative Q_3 mode stabilizes the *xy* orbital relative to a degenerate *zx* ± *iyz* orbital. A partially occupied *zx* ± *iyz* orbital in the low-spin t^5 configuration allows spin-orbit coupling. Either the on-site correlation U or the SO coupling further splits the degenerate band so as to make pPv $CaIrO_3$ an insulator. The strong SO coupling mixes up xy and degenerate *zx* ± *iyz* orbitals [44]. However, the local distortions determine the final combination of isospin states [7]. We have made a structural comparison with other Pv and pPv phases of $CaMO_3$ (M= Ru, Rh, and Pt) in Table 3. The pPv $CaPtO_3$ is a non-magnetic insulator with all the t orbitals occupied. A small octahedral-site distortion with $Q_3 = -1.155*10^{-3}$ reflects the intrinsic local distortion in the pPv structure. As a feedback effect of the strong orbital-lattice interaction, the structural distortion is clearly enhanced in the pPv $CaRuO_3$ ($Q_3 = -1.062*10^{-1}$), the pPv $CaRhO_3$ ($Q_3 = -6.466*10^{-2}$), and the pPv $CaIrO_3$ ($Q_3 = -8.741*10^{-2}$), where the component of *zx* ± *iyz* orbital is high in the final mixture of the wave function. This local structural distortion supports an unquenched orbital angular momentum L in the pPv $CaMO_3$ (M= Ru, Rh, and Ir) phases.

The pPv phase of $Ca_{1-x}Sr_xIrO_3$. The pPv structure is likely to occur where the geometric tolerance factor is much less than 1. The range of the t factor in which the pPv phase can be stabilized under high pressure is not yet clear. The t factor increases as x increases in

$Ca_{1-x}Sr_xIrO_3$. We have explored the upper limit of x within which the pPv phase is obtained. Fig.4 shows XRD patterns of the high-pressure phases of $Ca_{1-x}Sr_xIrO_3$ ($0 \leq x \leq 1.0$) samples. Except for a small amount of Ir metal, a pure pPv phase can be obtained for $x \leq 0.2$. For x = 0.3, a perovskite phase appears as a secondary phase in addition to the main pPv phase; a refinement of the XRD pattern for the sample prepared under 4 GPa shows that the ratio of pPv to Pv is 64: 36. This phase ratio increases to 73% pPv versus 27% Pv for a sample x = 0.3 prepared under 9 GPa. This result confirms that high pressure favors the pPv phase versus the Pv phase, but a pressure P = 9 GPa is not sufficient to have 100 % pPv phase for this composition. The unit-cell parameters of the pPv samples from the refinement are displayed in Fig.5(a). All of the parameters increase linearly with increasing Sr content; the same lattice expansion effect as a function of $\langle r_A \rangle$ has been seen in the perovskite structure, see for example, $Ca_{1-x}Sr_xMnO_3$ [45]. From a linear extrapolation of V versus x from samples $x \leq 0.2$, we can calculate the actual Sr content in the pPv phase to be 0.29 and 0.294 for the nominal x = 0.3 samples prepared under 4 and 9 GPa, respectively. The actual solid solution increases at the third decimal place when the synthesis pressure nearly doubles, which indicates that x = 0.3 is close to the upper limit for the pPv phase regardless of synthesis pressure. XRD for the substituted samples were performed with a laboratory X-ray diffractometer. During the Rietveld refinement on these XRD patterns, we had to open the option of a preferred orientation along the [101] axis in order to describe the XRD patterns properly for the pPv $Ca_{1-x}Sr_xIrO_3$ samples with x > 0. Because of this problem, we could not refine accurately the oxygen positions, *i.e.*, O_1 at 4c (0, *y*, 0.25) and O_2 at 8f (0, *y*, *z*), thus preventing us from obtaining reliable Ir-O bond lengths and Ir-O-Ir bond angles based on these XRD data of the substituted samples with the pPv structure.

The Pv phase of $Ca_{1-x}Sr_xIrO_3$. All high-pressure synthesis under 4 GPa resulted in a mixture of the Pv and pPv phases within $0.3 < x < 0.6$ and the volume ratio of the Pv phase grows as a function of x. For $x \geq 0.7$, pure Pv phases were obtained. The 6H polytype structure is formed instead of the Pv phase for these compositions if the synthesis was made under ambient pressure. The lattice parameters of the Pv samples are displayed in Fig.5(b). With increasing x in $Ca_{1-x}Sr_xIrO_3$, the parameters *a*, *c*, and *V* increase linearly whereas *b* decreases gradually until it crosses *a* at x ≈ 0.85. The *Pbnm* space group retains $b > a$ if the octahedra stay rigid. Such a crossover of *a* and *b* has been observed universally in the orthorhombic perovskite oxides due to the octahedral-site distortion.[1] From a linear extrapolation of V versus x from samples $x \le 0.2$ and $x \ge 0.7$, we can calculate the actual Sr content in the nominal x = 0.5 sample to be 0.26 for the pPv phase and 0.62 for the Pv phase, respectively. High pressure plays a sharply different role in the synthesis of $Ca_{1-x}Sr_xIrO_3$ samples for different domains of x; it stabilizes the pPv phase versus the Pv phase on the side of $CaIrO_3$ whereas the Pv phase is preferred under pressure relative to the 6H phase on the side of $SrIrO_3$.

II. Transport properties

The Pv phase of $CaIrO_3$ is a Pauli paramagnetic metal. The relatively high resistivity at room temperature and a weak upturn at low temperatures in Fig.6 could be attributed to the grain-boundary effect since the polycrystalline sample cannot be sintered at high temperatures. In comparison, a rectangular sample bar of the Pv phase of $SrIrO_3$ cut directly from the high-pressure product shows a typical metallic behavior. In contrast, the pPv phase $CaIrO_3$ is a wide-gap semiconductor. A measurement with the standard four-probe method can only be made down to about 200 K before it behaves like an open circuit. The same problem has also been indicated in the results by Ohgushi *et al* [34]. Sr doping creates a mixture of the pPv and the Pv phases for $0.3 \le x \le 0.5$. Within the Pv phase, Ca substitution changes $SrIrO_3$ from a metallic phase to an insulator phase. Therefore, both the pPv and the Pv phases in the mixed phase region for $0.3 \le x \le 0.5$ remain insulating. We have measured the transport properties of the pPv $CaIrO_3$ under hydrostatic pressure to 2 GPa. From a linear fit of lnR versus 1/T for pPv $CaIrO_3$ in Fig.7, we obtained an activation energy $E_a \approx 186$ meV which is consistent with $E_a \approx 170$ meV reported by Ohgushi *et al.* [34] We have also found that E_a is essentially pressure-independent.

The change from a metal to an insulator associated with the Pv-pPv structureal transition has also been seen in single-valent $CaRuO_3$ [46] [47] and $CaRhO_3$ [48] [31].The insulator phase can be attributed to a band narrowing in the quasi-2D structure of the pPv phase, which in turn enhances the SO coupling. It is pertinent to compare the Pv-pPv transition with a similar metal-insulator transition in connection with the structural change from the one-layer 214 phase of the Ruddlesden-Popper series to the perovskite structure. Whereas a metallic phase is found in the Pv phase of $SrVO_3$ [49], $CaRuO_3$ [46], $SrIrO_3$ (see Fig.6 of this work), the corresponding 214 phases are all insulators [50] [51] [52]. Therefore, the band narrowing effect in the quasi 2D structure is a common character in these layered oxides and is likely to be the origin of the insulator character of the pPv phase.

The dramatic difference in the electronic states of the Pv and pPv phases of $CaIrO_3$ is also reflected in the thermoelectric power S(T) shown in Fig.8. Similar to the resistivity measurement, the S(T) data of the pPv phase can only be recorded down to about 180 K before its magnitude fluctuates over a broad range. A significantly high S(300 K) ~ 400 μV/K and its temperature dependence for T > 180 K indicate that the pPv phase is an intrinsic semiconductor. In contrast, the metallic Pv phase has S ~ -22 μV/K at room temperature, which is reasonable for a metal. However, instead of showing the Mott diffusive formula found in most metals, i.e. |S| ~ T, |S| exhibits a huge hump as temperature decreases. The $|S|_{max}$ occurs at 170 K, which is too high for a phonon-drag effect [53]. As temperature decreases further, S crosses zero twice at T > 4.2 K. The hump of |S| at 170 K is similar to the thermoelectric-power enhancement found in the superconductive mixed-valent system $La_{2-x}Sr_xCuO_4$ [54]. The low-temperature behavior of S(T) can be interpreted as a positive peak due to a phonon-drag effect that is superimposed on a gradually changed, negative S(T). A hump of |S| similar to that of the Pv $CaIrO_3$ in Fig.8 has been found in the metallic Pv phase of $Ca_{1-x}Sr_xIrO_3$. However, the phonon-drag effect is reduced dramatically in the Pv $SrIrO_3$ and vanishes in the solid solution between $CaIrO_3$ and $SrIrO_3$ since chemical substitutions always enhance phonon scattering and therefore reduce the mean-free path of phonons. Whether the Pv $CaIrO_3$ is a "bad metal" as found in high-T_c cuprates and some 4d and 5d oxides remains to be confirmed by measurements on a single crystal sample. However, the thermoelectric power of Fig.8 indicates clearly that it is an anomalous metal.

III. Magnetic properties and critical behaviors near T_c

Magnetic susceptibility and magnetization data. As shown by the magnetic susceptibility $\chi(T)$ in Fig.9 (a,b) and the resistivity in Fig.6, the Pv phases of the entire $Ca_{1-x}Sr_xIrO_3$ system synthesized under high pressure are Pauli paramagnetic metals. Since high pressure destabilizes the Pv phase of $CaIrO_3$, we have to use the wet-chemical method to synthesize the Pv $CaIrO_3$. We have obtained 98.5% Pv phase $CaIrO_3$ plus some impurities like Ca_2IrO_4 and IrO_2 with the wet chemical method. The upturn in $\chi(T)$ of Pv $CaIrO_3$ below 90 K and the separation of the ZFC $\chi(T)$ from the FC $\chi(T)$ below about 40 K can be attributed to the minor phase Ca_2IrO_4, which exhibits an antiferromagnetic transition at T_N = 83.5 K.[38] This feature has also bee seen in the Pv phase of $Ca_{0.3}Sr_{0.7}IrO_3$. All the pPv $Ca_{1-x}Sr_xIrO_3$ ($0 \leq x \leq 0.3$) samples in Fig.9 (c,d) exhibit a weak ferromagnetism below T_c that decreases with increasing x. However, a nearly temperature-independent $\chi^{-1}(T)$ in the paramagnetic pPv phase at T > 300 K gives a non-physical Weiss constant and μ_{eff}. Violation of the C-W law is evidence of a strong single-ion anisotropy associated with SO coupling. As T_c is approached from $T > T_c$, $\chi^{-1}(T)$ shows a curvature that is opposite to that due to critical fluctuations found in a regular ferromagnet. As temperature increases from T_c, $\chi^{-1}(T)$ shows a shoulder-like temperature dependence. This gradual slope change in $\chi^{-1}(T)$ should be distinguished from that found in a regular canted-spin antiferromagnet in which a Curie-Weiss law is fulfilled at $T > T_N$ and a much sharper slope change is associated with T_N.

As shown in the schematic drawing of Fig.10, spin-spin exchange interactions in the pPv structure are made mainly through two different pathways, i.e. the virtual charge transfer (VCT) between Ir^{4+} along the edge-shared rows and the VCT through corner-shared oxygen O_1. The former gives a ferromagnetic coupling according to the superexchange rules whereas the second is problematic since the $Ir^{4+} - O_1 - Ir^{4+}$ bond angle θ =134.48 ° is just between 90° and 180°. A $\theta \leq 135°$ is likely to contribute to ferromagnetic coupling between edge-shared rows in pPv $CaIrO_3$. This argument is supported by the relationship of T_c versus the cell volume V in Fig.11. The $\langle r_A \rangle$ increase not only expands the cell volume, it also reduces the octahedral-site tilting angle as is found generally in orthorhombic perovskites. If this correlation holds in the pPv structure, the Sr doping in the pPv $Ca_{1-x}Sr_xIrO_3$ increases θ so as to weaken the ferromagnetic coupling through Ir^{4+} - O_1 - Ir^{4+} bonds. Unfortunately, the pPv phase becomes unstable against the Pv phase at $x \approx 0.3$, which makes it impossible to see an evolution from a weak ferromagnetism to an antiferromagnetism in pPv $Ca_{1-x}Sr_xIrO_3$. We can further test the relationship between crystal structure and magnetic properties in the pPv phase by measuring the magnetization under high pressure. In order to make a direct comparison between the pressure effect and the Sr substitution in pPv $CaIrO_3$, we show in Fig.11 the lattice parameters of the pPv $CaIrO_3$, normalized to those under ambient pressure, as a function of pressure P together with the normalized lattice parameters of the Sr substituted samples. The interlayer distance in the pPv structure, as measured by the lattice parameter *b,* is more sensitive to either P or x than are the lattice parameters *a* and *c*. Whereas the pressure-induced lattice-parameter changes are just opposite to those induced by the Sr substitution, T_c shows no visible change under pressure. In comparison, T_N (T_c) is sensitive to both pressure and the lattice expansion by increasing $\langle r_A \rangle$ in the orthorhombic perovskites $AMn^{4+}O_3$ (A= alkaline earth) [45 55] and $RM^{3+}O_3$ (R = rare earth, M = Ti, V, Mn, Fe) [56 57]. Although the slope in the curve of T_N (T_c) versus cell volume changes sign at the turning point from the pressure-induced change to the $\langle r_A \rangle$-expansion-induced change in the Pv phases, the change of T_N (T_c) on both sides can be rationalized by considering both the octahedral-site rotations and the local site distortions. T_N (T_c) in the orthorhombic perovskites changes monotonically as a function of the rotations and local site distortions. The plots of $T_c(T_N)$ versus P and $\langle r_A \rangle$ in Fig.11 distinguish clearly the pPv $CaIrO_3$ from most magnetic perovskites. A structural study under pressure on the pPv $CaIrO_3$ is under way in order to see whether the local structure of the pPv phase responds to pressure in a different way from what we have seen in the Pv structure.

Fig. 12 shows the isothermal magnetization of pPv $CaIrO_3$. We highlight first a few important characteristics from these curves before turning to their possible interpretations: (a) like a regular ferromagnet, the magnetization, i.e. a non-linear M-H curve and the onset of a coercive field H_c, appears abruptly at $T < T_c$; (b) the remanant moment as measured by the difference $\Delta M = M_R^+ - M_R^-$ increases as temperature decreases within the range $70\ K < T < T_c \approx 115\ K$; (c) whereas the magnetization loops within ± 5 T are similar, ΔM reduces dramatically as temperature decreases below 70 K and the entire loop moves vertically to a totally positive magnetization at $T < 30$ K. Although effort has been taken to have a zero-field cooling (within ± 0.5Oe) for the measurements in Fig.12, whether the entire magnetization loop is located at positive or negative magnetization depends very sensitively on the small unbalanced field in the magnet of a SQUID magnetometer as the sample was cooled through T_c. We have measured the influence of the field-cool effect through T_c on the loop at 5 K and we show the results in Fig.13. Interestingly, although the eventual location of the loop along the magnetization axis is determined by the small magnetic field as the sample is cooled through $T_{c,}$ a magnetic field as high as ± 9 T is insufficient to alter the loop at lower temperatures such as $T = 5$ K. The unusual magnetization should be distinguished from that caused by the *exchange-bias* effect where the coexistence of ferromagnetic and antiferromagnetic couplings at interfaces causes the entire loop to shift horizontally from the origin in an M-H plot [58].

Magnetization interpretation. The whole loop shifting vertically can be interpreted by a low-H_c magnetization loop (LHML) superimposed on a high-$H_{c'}$ magnetization loop (HHML), say $H_{c'} \sim 30$ T. A HHML would be associated with a magnetization reversal of orbital moments below $T_t \sim 70\ K < T_c$. The domain walls associated with the pinned orbital moment at $T < T_t$ are narrow and not easily moved; they have a totally different dynamics than the conventional domain walls associated with interatomic spin-spin interactions. As shown by the schematic drawing of Fig.10, the orbital moments are directed to O_1 in each octahedron due to the local lattice distortion, but their sign fluctuates at $T > T_c$ and can be changed in a laboratory H field at $T_t < T < T_c$. The strong SO coupling gives an anomalous paramagnetic susceptibility, but the M-H loop is conventional in the interval $T_t < T < T_c$. Once the orbital moments are ordered within magnetic domains below T_t, only an enormous applied H can move the domain walls. On the other hand, the interatomic spin-spin interaction tries to stabilize a collinear ferromagnetic spin ordering below T_c. Canting of the Ir-O_1 bond direction creates a competition between spin canting and the spin-spin exchange. Spins become locked strongly to the orbital moments below T_t due to the SO coupling. The degree of freedom for spin rotation is significantly reduced, so that a magnetic-field excursion $\Delta H = \pm 5$ T can only reorient a small component of the total spin magnetization, shown as the LHML, that is superimposed on the magnetization associated with a fixed orbital-domain structure. It is important to know that the coupling between the orbital moments is weak; therefore, the direction of the orbital moments become ordered only below T_c where the Weiss-molecular field from the spin ordering is present. However, the domain walls associated with the orbital moments are extremely sensitive to a small deviation (± 100 Oe) from zero field at T_c. Below T_t, the domain wall structure for the orbital moments cannot be changed even with a magnetic-field excursion $\Delta H = \pm 9$ T at T = 5 K.

As the orbital moments are random above T_c, the SO coupling only makes invalid the Curie-Weiss law in the paramagnetic phase. Ferromagnetic spin-spin ordering induces ordering of the orbital magnetic moments; which have their directions pinned to the local structural distortion that, in turn, locks up the spin orientation below T_c. However, a small component of the spins perpendicular to the Ir-O_1 axes is coupled ferromagnetically by the spin-spin interactions, which provides the LHML loop having a magnitude that decreases on lowering the temperature. Thus, the M-H loops of Fig.12, 13 reveal an interesting competition between orbital-lattice, intraatomic spin-orbit, and interatomic spin-spin interactions.

<u>Critical behavior.</u> Critical behavior near T_c provides important information about the spin-spin interactions. A second-order ferromagnetic transition near T_c can be

characterized by a set of critical exponents [59], *i.e.* β, γ, and δ. They are associated with the spontaneous magnetization $M_s(T) \equiv M(H = 0, T)$, the magnetic susceptibility $\chi_0(T) \equiv \partial M / \partial H|_{H=0}$, and the critical isotherm $M(T_c, H)$, respectively, and are defined by the power-law dependence of the reduced temperature, $t \equiv (T-T_c)/T_c$, or magnetic field H, *viz.*

$$M_s(T) \propto |t|^{\beta}, \qquad t < 0; \tag{2}$$

$$\chi_0^{-1}(T) \propto |t|^{\gamma}, \qquad t > 0; \tag{3}$$

$$M(T_c, H) \propto H^{1/\delta}, \qquad t = 0. \tag{4}$$

For a ferromagnet with critical behavior close to that of the mean-field model, the $M_s(T)$ and $\chi_0^{-1}(T)$ can be determined by extrapolating high-field ($H > 1$ T) isotherms in the plot of M^2 versus H/M to either the M^2 or the *H*/*M* axis. As shown in Fig.14, an Arrott plot [60] of the magnetization data of the pPv $CaIrO_3$ gives nearly linear isotherms. The temperature dependence of the M_s and χ_0^{-1} along with their power-law fitting curves are displayed in Fig.15(a). The critical exponents determined from the curve fitting were $\beta = 0.42(1)$ with $T_c^- = 108.15(2)$ K and $\gamma = 1.11(2)$ with $T_c^+ = 108.19(7)$ K. Alternatively, more accurate critical exponents of $\beta = 0.444(6)$ and $\gamma = 1.043(9)$ can be obtained by linear fittings to curves in the plots of $\log(M_s)$ versus log t and $\log \chi_0^{-1}$ versus log t with $T_c = 108.2$ K in Fig.15(b) according to Eq. (2) and (3). Moreover, as shown in Fig.15(c), the slope of the isothermal magnetization at the critical temperature $T_c = 108.2$ K in the plot of log M versus log H can be estimated from interpolating slopes at neighboring temperatures T = 108 K and 109 K; a $\delta = 1/\text{slope} = 3.31(3)$ is obtained. These critical exponents satisfy excellently the Widom scaling relation [61], *viz.* $\delta = 1 + \gamma/\beta$.

As a further test of the critical exponents and T_c that we have obtained from previous plots and their analysis, we compare our data to the prediction of the scaling hypothesis:

$$M(H, t) = |t|^{\beta} f_{\pm}(H/|t|^{\beta+\gamma}), \tag{5}$$

where f_+ for $T > T_c$ and f_- for $T < T_c$ are regular analytical functions. Equation (5) implies that the $M/|t|^{\beta}$ as a function of $H/|t|^{\beta+\gamma}$ produces two universal curves: one for $T < T_c$ and the other for T > T_c. With the values of the critical exponents $\beta = 0.444$ and $\gamma = 1.043$ and a critical temperature $T_c = 108.2$ K obtained above, the scaling plots of the M(H) data for H > 0.5 T are displayed in Fig.16. All the points indeed fall on two curves. The goodness of the scaling can be seen more clearly in the log-log plots as an inset of Fig.16, which implies that the critical analysis in this study is reliable.

The Stoner-Wohlfarth (SW) [62, 63] and the Heisenberg models [64] describe two extreme cases of ferromagnetism. Very weak magnetization and a metallic ground state are essential for the SW model to justify parallel linear isotherms in the Arrott plot; this condition is found, for example, in the very-weak itinerant-electron ferromagnet $ZrZn_2$ [65], which gives the mean-field universality class with $\beta = 0.5$, $\gamma = 1.0$, and $\delta = 3.0$.[64] On the other hand, Heisenberg ferromagnetism can occur in either metals or insulators with localized spins; linear isotherms can be realized in a modified Arrott plot [66], *i.e.*, $M^{1/\beta}$ vs $(H/M)^{1/\gamma}$, with β and γ close to 0.365 and 1.386, respectively. A large number of known ferromagnets [67] [68] [69] [70] [71] [72] belong to this universality class. The critical exponents of the pPv $CaIrO_3$ are compared with those predicted by the mean-field and 3D Heisenberg models [64] and illustrated by their representative ferromagnets [65] [67-72] in Table 4; the data indicate that pPv $CaIrO_3$ should belong to the mean-field universality class. A recent study [73] on the critical behavior of the 9R $BaIrO_3$ showed that the critical exponent γ = 1.03(3) for T > T_c is also close to that predicted by the mean-field theory, although the values of β = 0.82(3) and δ = 2.20(1) for T ≤ T_c do not belong to any universality class. As far as we know, the pPv $CaIrO_3$ is the first case of a Mott insulator showing the mean-field critical behavior. Since the 9R $BaIrO_3$ shows a critical behavior similar to that of the pPv $CaIrO_3$, it is useful to find common features in these two iridates. As shown in the previous section, the intrinsic structure of the pPv structure leaves the orbital moment unquenched in $CaIrO_3$. The 9R $BaIrO_3$ has a more complicated structure; there are four Ir^{4+} sites. A structural study [37] has shown that the orbital moment is not quenched at sites Ir(2) and Ir(4). The mean-field or close-to-mean-field behavior in these two systems occurs in a narrow temperature range around T_c, but below the temperature where either orbital moments become magnetized or a CDW phase is formed. The magnetization of orbital moments causes the M-H loop to shift vertically away from the origin, which has been seen in both systems [74]. The crystal structure also gives a staggered easy magnetization axis in the 9R $BaIrO_3$. Both systems show a very weak magnetization. The strong SO coupling and staggered easy axis are key factors contributing to the weak magnetization, which may be ultimately required to justify the mean-field critical behavior [75].

IV. Thermal conductivity and lattice dynamics

The distorted perovskite $MgSiO_3$ undergoes a phase transition to the pPv structure under high pressure and high temperature, which has been believed to be the main form of matter in the D'' layer of the Earth's lower mantle. The formation of the D'' layer marks the evolution from the baby Earth to the mature Earth. [76] The high thermal conductivity in the D'' layer has been thought to transfer heat more efficiently from the Earth core to the Earth mantle [76]. It is very important to verify this argument. However, the pPv phase $MgSiO_3$ cannot be quenched to ambient pressure. It remains a great challenge to carry out an *in-situ* measurement of the thermal conductivity κ or thermal diffusivity D on the pPv $MgSiO_3$. The availability of the pPv phase $CaIrO_3$ and a series of samples $Ca_{1-x}Sr_xIrO_3$ showing a continuous evolution from the pPv phase to the Pv phase provide an excellent opportunity for us to demonstrate the thermal conductivity in the pPv phase and, most importantly, to compare with the Pv phase consisting of nearly the same elements.

Fig.17(a) shows the temperature dependence of κ for the whole $Ca_{1-x}Sr_xIrO_3$ system. The pPv $CaIrO_3$ shows a surprisingly high thermal conductivity at room temperature that decreases continuously in the region of mixture of the pPv and Pv phases and finally in the Pv phase. We have plotted κ(300K) versus x in Fig.17(b). As far as we know, κ of the pPv $CaIrO_3$ at room temperature is the highest among all perovskite oxides. The Pv $SrIrO_3$, the end phase in this phase diagram, shows a κ that is comparable to other perovskite oxides. It is also normal that κ in the chemically substituted samples is lower than that without the substitution. All samples show that κ increases as temperature decreases as expected for the phonon thermal conductivity. Therefore, we have applied the Debye model for analysis of κ(T) from the pPv and Pv samples.

Since pPv $CaIrO_3$ is an insulator and the electronic contribution in the Pv $SrIrO_3$ and the Ca substituted Pv samples is negligible, we discuss only the lattice contribution. The thermal conductivity is related to the specific heat C, the mean phonon velocity υ and the phonon mean-free path ℓ by the expression $\kappa = (1/3)C\upsilon\ell$. Fig.18 shows that the specific heats C_p are similar for all the samples $Ca_{1-x}Sr_xIrO_3$ including the pPv phase, a mixture of the pPv and the Pv phases, and the Pv phase. They are actually heavily overlapped. Given that C_p for the pPv phase is normal, we turn to υ and ℓ. The results of specific heat also provide Debye temperatures θ_D calculated through the Debye formula embedded in the PPMS system, which is related to the mean phonon velocity υ. The phonon contribution to thermal conductivity $\kappa_{ph}(T)$ can be described with the Debye model [77]:

$$\kappa_{ph}(T) = \left(\frac{k_B}{2\pi^2\upsilon}\right)\left(\frac{k_B}{\hbar}\right)^3 T^3 \int_0^{\theta_D/T} \frac{x^4 e^x}{\left(e^x - 1\right)^2}\tau(\omega,T)dx \quad , \tag{6}$$

where $x = \hbar\omega / k_B T$ and $\tau(\omega,T)$ is the relaxation time of a phonon, which can be expressed as

$$\tau^{-1} = \upsilon/L + A\omega^4 + B\omega^3 T\exp(-\Theta_D/bT) \tag{7}$$

The first term in Eq.(7) is related to phonon scattering at the sample's boundary, the second is at defects, and the third is phonon-phonon scattering. The phonon-phonon scattering dominates κ at high temperatures whereas the effects due to scatterings at the sample's boundary or at impurities become obvious at low temperatures. As shown in Fig.19, the overall curve fittings to the Debye model are reasonable and fitting parameters are listed in Table 5. The parameter L is related to the phonon scattering at grain boundaries. This parameter shows no obvious change within the whole series of samples, but is smaller by four orders of magnitude than that for the single crystal $Ca_3Co_2O_6$.[78] This change makes sense given that all iridates in this study are ceramic samples. The most obvious change in these fitting parameters on crossing from the pPv to the Pv phases is the phonon-phonon scattering parameter *b*, which is significantly smaller in the pPv phase, especially in the pPv $CaIrO_3$. In order to distinguish whether the significantly reduced phonon-phonon scattering in the pPv phase is related to peculiar bonding and symmetry in the structure or something associated with Ir(IV) placed at an octahedron with a $-Q_3$ deformation, we have synthesized the pPv $CaPtO_3$ under high pressure. As shown in Fig.19, the overall κ(T) of the pPv $CaPtO_3$ is glassy and κ(300K) is even lower than that of Pv $SrIrO_3$. Since the thermal conductivity in a solid-state sample is highly sensitive to factors such as impurities, vacancies, and lattice strain, κ of the pPv $CaPtO_3$ may not be typical. Therefore, it is still too early to rule out the first possibility that the pPv structure can have a generally high κ. However, the issue of orbital ordering is equally important to influence the phonon-phonon scattering; we need also to consider the feedback effect of strong orbital-lattice interaction on the local distortion and therefore κ.

The interplay between orbital-orbital, spin-spin, and spin-orbital (not the onsite $\lambda\mathbf{L}\cdot\mathbf{S}$) interactions makes a rich phase diagram for the perovskites RVO_3. Although long-range intrinsic local structural distortions lift the orbital degeneracy, the orbitals remain disordered or in an orbital liquid state at temperatures $T > T_{oo}$. A much reduced and glassy κ is found in the orbital-disordered state of the RVO_3 perovskites. The orbital order-disorder transition at T_{oo} has been sensitively picked up by measurement of the thermal conductivity.[79] However, full orbital ordering only occurs below the orbital flipping transition at $T_{CG} < T_{oo}$, to restore finally a normal phonon thermal conductivity in RVO_3. What we have seen in pPv $CaIrO_3$ is an anomalously higher κ at room temperature than the typical phonon thermal conductivity found in the perovskite $LaGaO_3$ (~ 5 W m^{-1} K^{-1}) or $LaAlO_3$ (~ 11 W m^{-1} K^{-1}), which means that pinning the orbital moment to the Ir-O_1 direction in pPv $CaIrO_3$ does something else to enhance κ other than by regular orbital ordering.

The axis of the orbital moments is locked up along the Ir-O_1 direction due to the structural bias effect. As a feedback effect of the strong orbital-lattice interaction, the significantly smaller bond-length ratio of (Ir-O_1)/(Ir-O_2) in pPv $CaIrO_3$ than that in pPv $CaPtO_3$ with low-spin t^6 configuration appears to boost the bonding strength of the Ir-O_1 bond, which is supported by a slightly higher Debye temperature θ_D in pPv $CaIrO_3$. The group velocity of the optical branches is small, so that optical phonons by themselves contribute negligibly to κ [77]. But they affect heat flow by interacting with the acoustic phonons, which are mainly responsible for the thermal conductivity. Strengthened Ir-O bonds result in a decreasing room-temperature population of optical phonons by lifting some optical branches to higher energy. A slightly reduced C_p of pPv $CaIrO_3$ at room temperature relative to that of the Pv phase is consistent with such a change in the phonon spectrum. Although a C_p reduction offsets $\kappa = (1/3)C_p\upsilon\ell$ a bit, decreasing the population of optical phonons reduces phonon-phonon scattering and therefore enhances significantly the thermal conductivity through a larger ℓ.

Conclusion

We have studied systematically irridates with the post-perovskite structure and compared them with the perovskite structure. Major results are listed as follows. (1) High-pressure synthesis up to 10 GPa can stabilize the post-perovskite phase in $Ca_{1-x}Sr_xIrO_3$ up to $x \approx 0.29$; a mixture of perovskite and post-perovskite phase has been obtained within $0.3 \leq x \leq 0.6$. High-pressure synthesis is required to stabilize the perovskite structure relative to the polytypes 6H structure for $0.7 \leq x \leq 1$. (2) The symmetry of the post-perovskite structure allows a tetragonally distorted octahedron. In contrast to the local distortion found in most K_2NiF_4 structures, the octahedral-site distortion in the post-perovskite structure can be generally described by a $-Q_3$ model, *i.e.* two short M-O bonds and four long M-O bonds as extracted from the low-spin post-perovskite $CaPtO_3$ with t^6e^0 configuration. This local distortion is dramatically enhanced in the post-perovskite $CaMO_3$ (M = Ru, Rh, Ir) where the t orbitals are not fully occupied. (3) The post-perovskite $CaIrO_3$ is a ferromagnetic insulator whereas the perovskite $CaIrO_3$ made from the wet chemical method is a Pauli paramagnetic metal. Sr substitution does not change the ground state in the post-perovskite $CaIrO_3$. The effect of chemical substitution on the structure and physical properties have been directly compared with the pressure effect made on the sample. The post-perovskite $CaIrO_3$ responds differently to chemical substitution and hydrostatic pressure than do in most perovskites. (4) The post-perovskite $CaIrO_3$ exhibits anomalous magnetic properties. Depending sensitively on a small magnetic field within -100 Oe < H < 100 Oe during a field cool through T_c, the magnetization M-H loop moves vertically from the origin. From the M-H loop made at different temperatures below T_c, an M-H loop with a high saturation but small coercive force observed right below T_c is distinguished from a loop with a low saturation moment but a huge coercive force (it is clearly larger than 9 T) as temperature is lowered further. The M-H loop with such a huge coercive force has not been seen in any magnets where ferromagnetism is due to spin-spin exchange interaction. Although the post-perovskite $CaIrO_3$ is an insulator, it exhibits the critical behavior near T_c that can be described nearly perfectly by a mean-field model. (5) The thermal conductivity is greatly enhanced in post-perovskite phase compared with that of the perovskite phase in the samples $Ca_{1-x}Sr_xIrO_3$. This finding is significant for explaining the role of the D" layer of post-perovskite $MgSiO_3$ in the overall Earth evolution.

Acknowledgment

This work was supported by NSF (DMR 0904282) and the Robert A Welch foundation (Grant F-1066).

Table 1 Atomic coordinates and isotropic thermal factors B_{iso} [Å^2] for Pv $CaIrO_3$ from the high-resolution XRD^a with synchrotron radiation at 295 K; Space group *Pbnm* (No.62), *a* = 5.35046(1), *b* = 5.59291(1), *c* = 7.67694(2) Å, *V* = 229.730(1) Å^3, Z = 4.

atom	site	*x*	*y*	*z*	B_{iso}(Å)
Ca	4*c*	-0.01403(37)	0.05962(14)	0.25	0.713(22)
Ir	4*b*	0.5	0.0	0.0	0.277(2)
O1	4*c*	0.10487(54)	0.47110(76)	0.25	0.924(94)
O2	8*d*	0.69257(43)	0.30488(43)	0.05602(30)	1.067(77)

[a] Discrepancy factors: R_p= 6.45%, R_{wp}= 8.75%, R_{exp}= 3.93%, χ^2= 4.97, R_{Bragg}= 3.46%.

Table 2 Atomic coordinates and isotropic thermal factors B_{iso} [Å^2] for pPv CaIrO$_3$ from the high-resolution XRD [a] with synchrotron radiation at 295 K; Space group *Cmcm* (No. 63), *a* = 3.14536(1), *b* = 9.86365(5), *c* = 7.29796(3) Å, *V* = 226.417(2) Å^3, Z = 4.

atom	site	*x*	*y*	*z*	B_{iso}(Å)
Ca	4*c*	0.0	0.24933(12)	0.25	0.853(20)
Ir	4*a*	0.0	0.0	0.0	0.503(3)
O1	4*c*	0.5	0.42240(33)	0.25	0.269(59)
O2	8*f*	0.5	0.12827(23)	0.05216(30)	0.309(45)

[a] Discrepancy factors: R_p= 7.26%, R_{wp}= 8.99%, R_{exp}= 3.76%, χ^2= 5.72, R_{Bragg}= 5.04%.

Table 3 Main interatomic distances (Å) and angles (°) of Pv and pPv forms of CaIrO$_3$ at 295 K. Data of CaRhO$_3$, CaRuO$_3$, Sr$_2$IrO$_4$, and CaPtO$_3$ are also shown for comparison.

	Pv		pPv	
CaIrO$_3$	Ir–O1 ×2	2.0061(9)	Ir–O1 ×2	1.9786(13)
	Ir–O2 ×2	2.020(2)	Ir–O2 ×4	2.0543(13)
	Ir–O2 ×2	2.038(2)		
	<Ir–O>	2.021	<Ir–O>	2.053
	Ir–O1–Ir	146.15(6)	Ir–O1–Ir	134.48(10)
	Ir–O2–Ir	144.95(9)		
	O1–Ir–O2	90.41(17)	O1–Ir–O2	93.86(12)
	O1–Ir–O2	91.11(15)	O2–Ir–O2	99.92(5)
	O2–Ir–O2	90.26(15)	Ir–Ir	3.14536(13)
[a]CaRhO$_3$	Rh–O1 ×2	2.007(3)	Rh–O1 ×2	1.950(2)
	Rh–O2 ×2	1.856(7)	Rh–O2 ×4	2.006(3)
	Rh–O2 ×2	2.134(6)		
	<Rh–O>	1.999	<Rh–O>	1.987
	Rh–O1–Rh	143.9(5)	Rh–O1–Rh	137.3(4)
	Rh–O2–Rh	149.6(4)		
[b]CaRuO$_3$	Ru–O1 ×2	1.979(5)	Ru–O1 ×2	1.947(2)
	Ru–O2 ×2	1.973(2)	Ru–O2 ×4	2.039(2)
	Ru–O2 ×2	2.008(5)		
	<Ru–O>	1.987	<Ru–O>	2.008
	Ru–O1–Ru	151.2(4)	Ru–O1–Ru	139.0(3)
	Ru–O2–Ru	150.6(3)		

[c]Sr_2IrO_4	Ir–O1 ×2	2.058(2)		
	Ir–O2 ×4	1.981(1)		
	<Ir–O>	2.007		
	Ir–O2–Ir	157.9 (1)		
[d]$CaPtO_3$			Pt–O1 ×2	2.016(3)
			Pt–O2 ×4	2.017(3)
			<Pt–O>	2.017
			Pt–O1–Pt	131.2(3)

[a] ref.30; [b] ref.29; [c] ref.80; [d] ref.32.

Table 4 Comparison of critical exponents of the pPv $CaIrO_3$ with those predicted by various theoretical models and obtained in a large number of itinerant and localized ferromagnets.

Materials	Ref.	T_c (K)	β	γ	δ	Transport property
pPv $CaIrO_3$[a]	This work	108.2(1)	0.444(6)	1.043(9)	3.31(3)	Insulator
Mean-field[d]	59	/	0.5	1.0	3.0	/
$ZrZn_2$[b]	65	27.50(5)	0.52(5)	/	3.20(8)	Metal
3D Heisenberg[d]	59	/	0.365(3)	1.386(4)	4.80(4)	/
Ni[a]	66	627.4	0.378(4)	1.34(1)	4.58(5)	Metal
CrO_2[c]	67	386.5	0.371(5)	1.43(1)	4.85	Metal
Sr_2FeMoO_6[b]	68	409.1	0.388(4)	1.30(1)	4.35	Metal
$La_{0.7}Sr_{0.3}MnO_3$[b]	69	354.0(2)	0.37(4)	1.22(3)	4.25(2)	Metal
$Pr_{0.73}Ca_{0.27}MnO_3$[b]	70	127.0(5)	0.36(2)	1.36(2)	4.81(2)	Insulator
La_2NiMnO_6[a]	71	270.3(2)	0.41(1)	1.30(2)	4.14(9)	Insulator
$YTiO_3$[b]	72	26.5	0.359(3)	1.440(5)	4.85(2)	Insulator

[a] Polycrystal; [b] Single crystal; [c] Thin film; [d] Theory

Table 5 Parameters in the curve fitting on κ(T) of $Ca_{1-x}Sr_xIrO_3$ with the Debye model.

x	0	0.1	0.2	0.3	0.5	0.7	0.8	0.9	1.0
θ_D (K)	607	614	568	551	523	413	504	527	556
A (10^{-40} s^3)	0.425	1.317	2.658	2.965	1.64	2.57	1.93	1.89	4.22
B (10^{-29} $K^{-1}s^2$)	1.66	1.98	2.91	2.85	7.99	1.49	2.12	1.23	4.18
b	3.7	38	6.4	8.75	59	49	76	20	18
L (10^{-8} m)	0.488	8.10	1.65	2.85	9.23	6.46	9.76	6.25	5.51

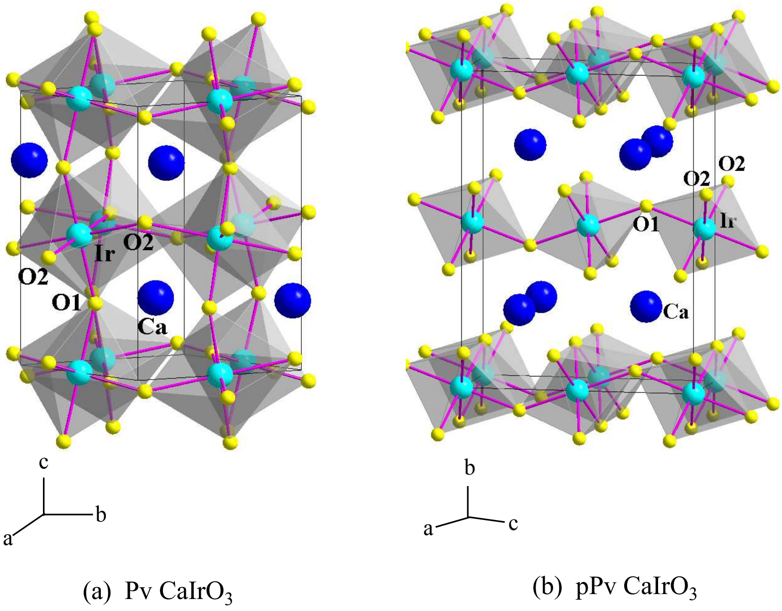

(a) Pv $CaIrO_3$ (b) pPv $CaIrO_3$

Fig.1 (Color online) Crystal structures of (a) Pv and (b) pPv $CaIrO_3$.

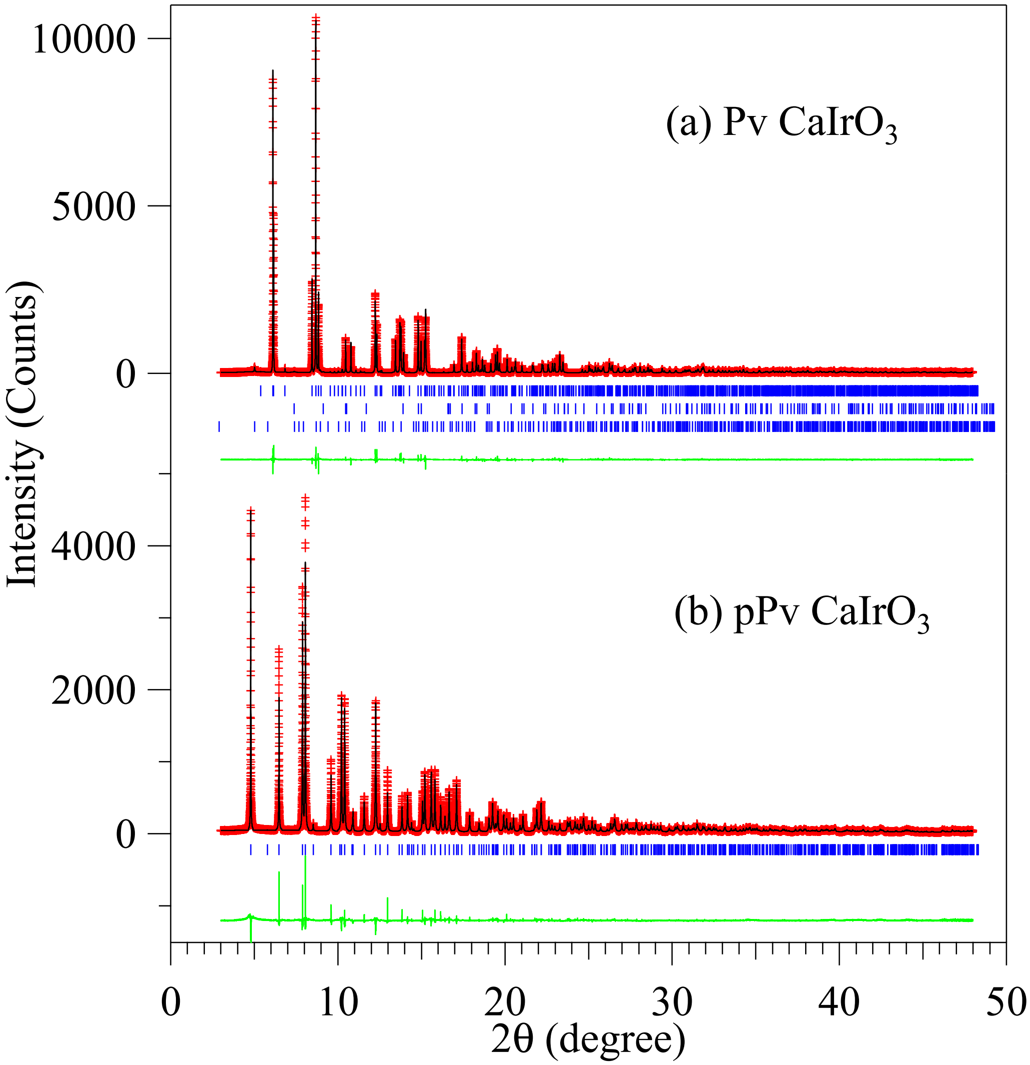

Fig.2 (Color online) Observed (cross) and calculated (solid line) high-resolution XRD profiles of the Pv and pPv $CaIrO_3$ measured at 295 K with synchrotron radiation (λ = 0.412207Å). Some impurity phases, 0.2% IrO_2 and 1.3% Ca_2IrO_4 in the sample of Pv $CaIrO_3$ have been determined from the refinement.

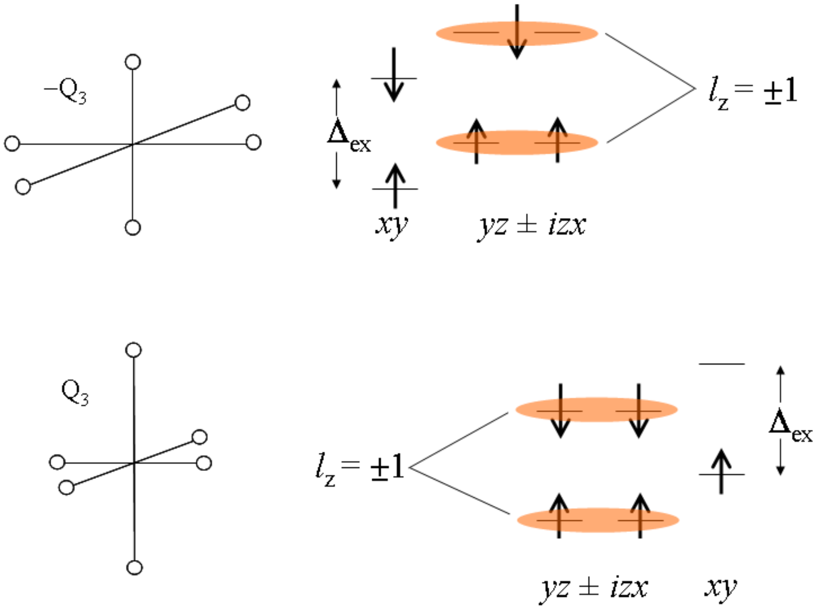

Fig.3 (Color online) Schematic diagram of octahedral-site distortion and orbital levels for the low-spin d^5 configuration without the spin-orbit coupling.

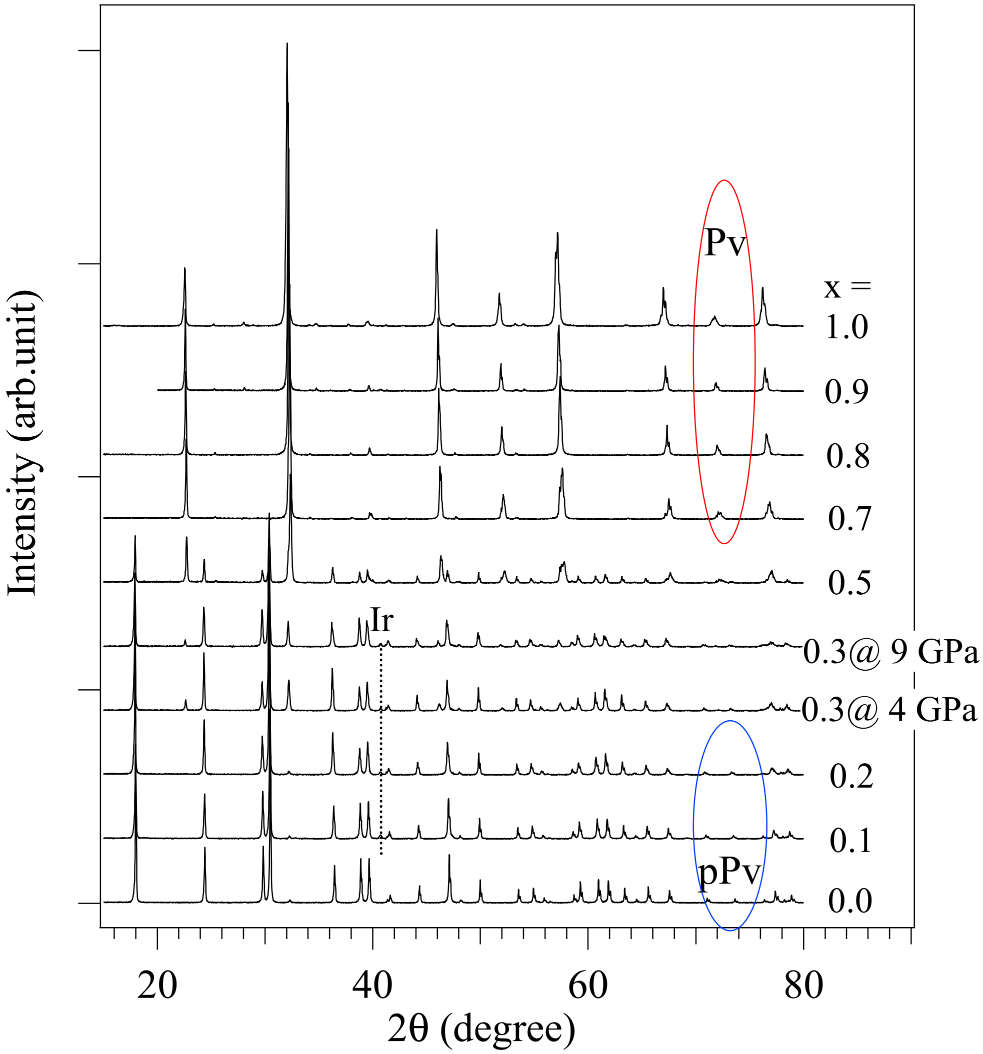

Fig.4 XRD patterns of the high-pressure phase of $Ca_{1-x}Sr_xIrO_3$.

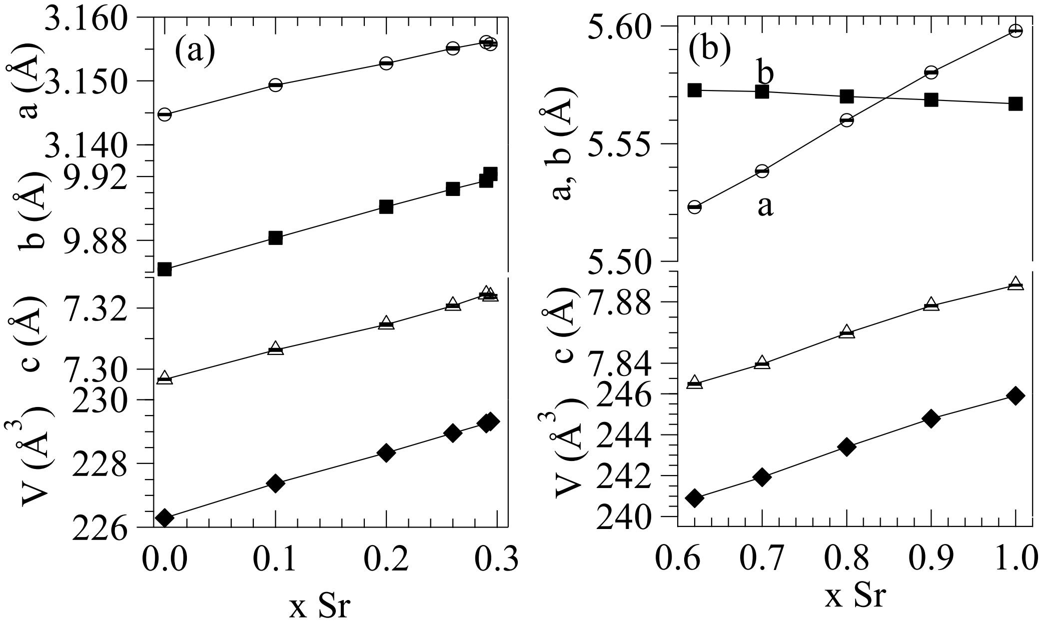

Fig.5 Lattice parameters as a function of x in the (a) pPv and (b) Pv $Ca_{1-x}Sr_xIrO_3$.

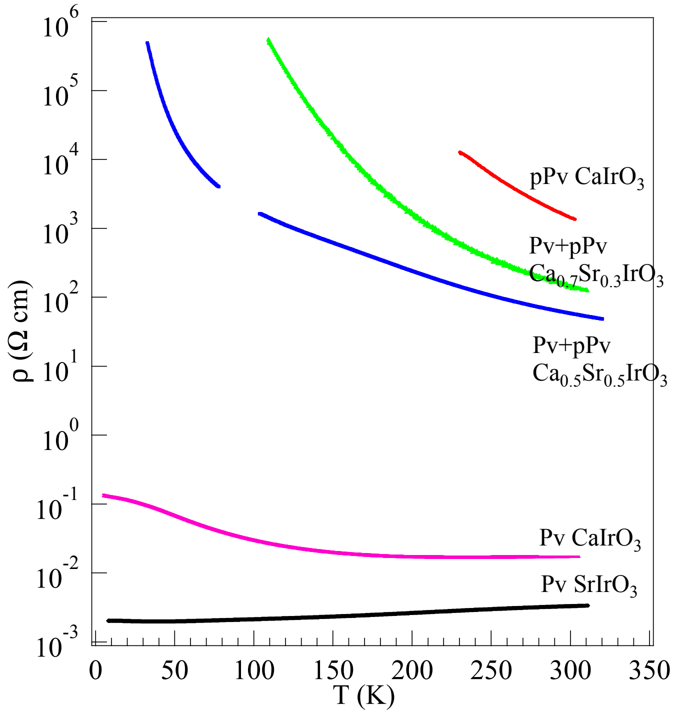

Fig.6 (Color online) Temperature dependence of resistivity in the pPv and the Pv $Ca_{1-x}Sr_xIrO_3$.

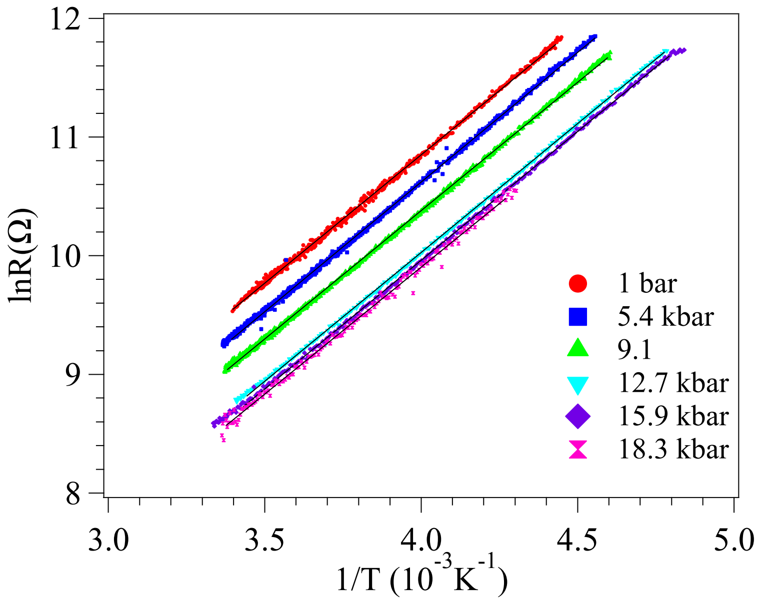

Fig.7 (Color online) Temperature dependence of resistance of the pPv $CaIrO_3$ under different pressures.

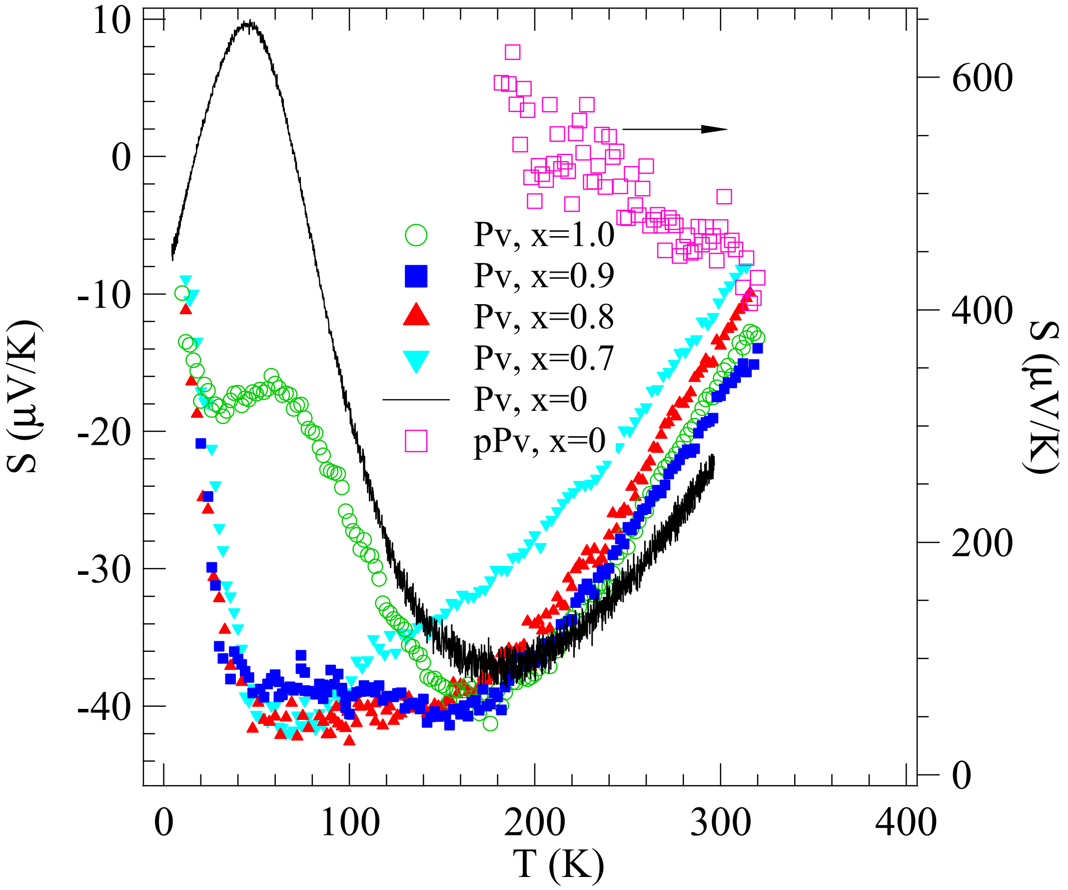

Fig.8 (Color online) Temperature dependence of thermoelectric power for the Pv and the pPv $Ca_{1-x}Sr_xIrO_3$.

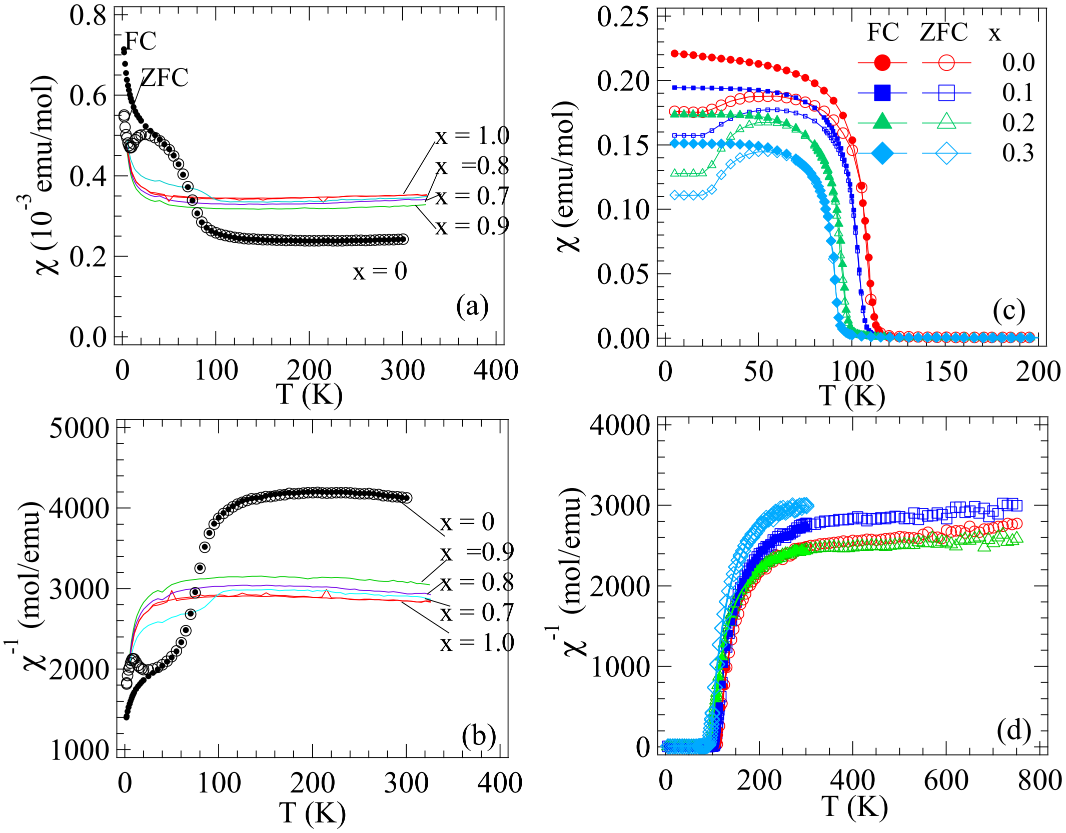

Fig.9 (Color online) Temperature dependence of magnetic susceptibility and inverse magnetic susceptibility for (a), (b) the Pv phase and (c) (d) the pPv phase of $Ca_{1-x}Sr_xIrO_3$.

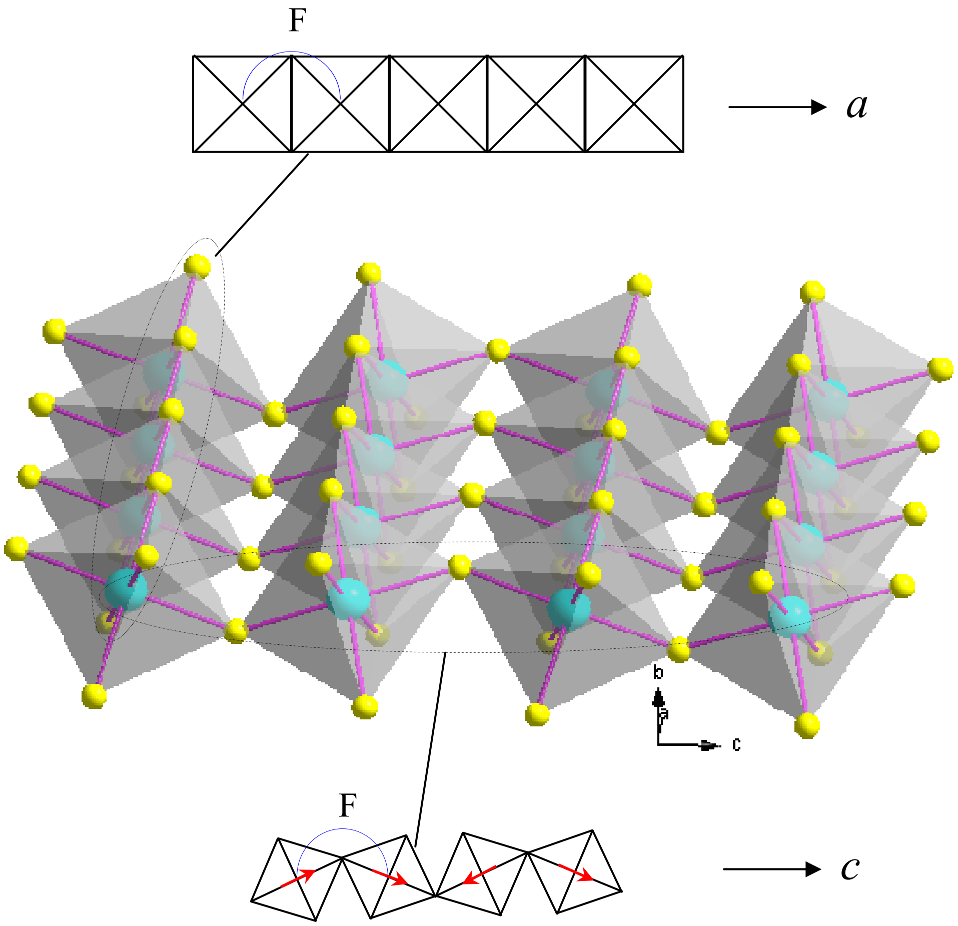

Fig.10 (Color online) Schematic drawing of the [010] layer and major pathways for the superexchange interactions in the pPv $CaIrO_3$. Arrows inside octahedra represent the orbital moment at room temperature.

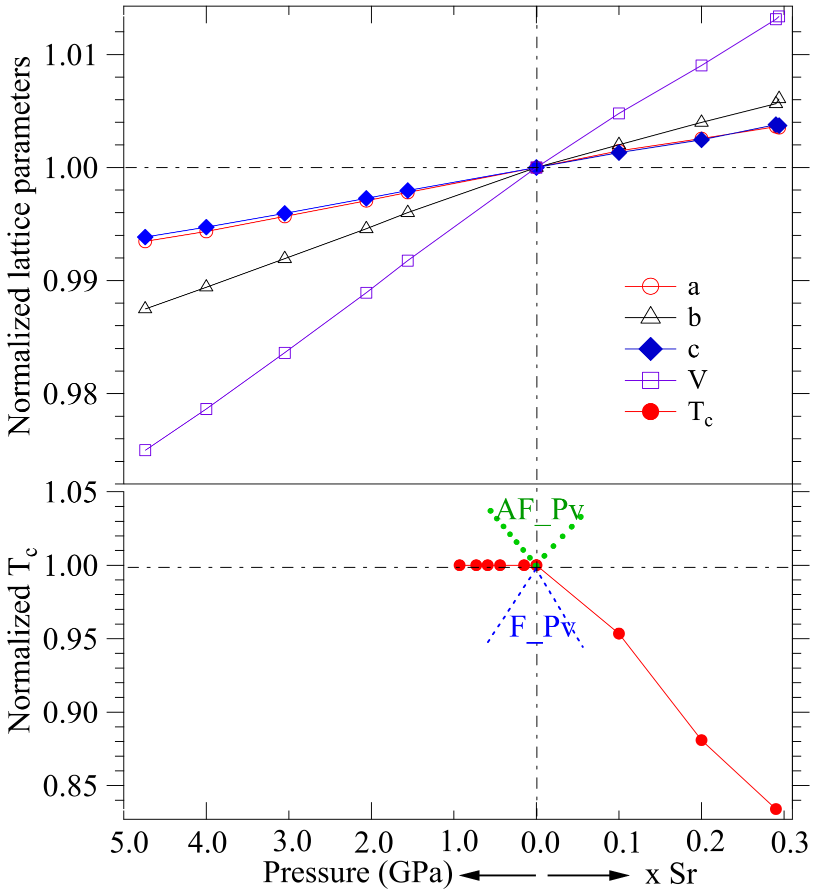

Fig.11 (Color online) Lattice parameters and magnetic transition temperature as a function of either x in the pPv $Ca_{1-x}Sr_xIrO_3$ or hydrostatic pressure in the pPv $CaIrO_3$. Dashed lines inside the plot show schematically the behavior of $T_c(T_N)$ as a function of either the lattice expansion or high pressure for magnetic perovskites. The structural data of pPv $CaIrO_3$ under pressure are from Ref. 22. A similar pressure effect on T_c of pPv $CaIrO_3$ has also been reported by Ohgushi *et al* in Ref. 36.

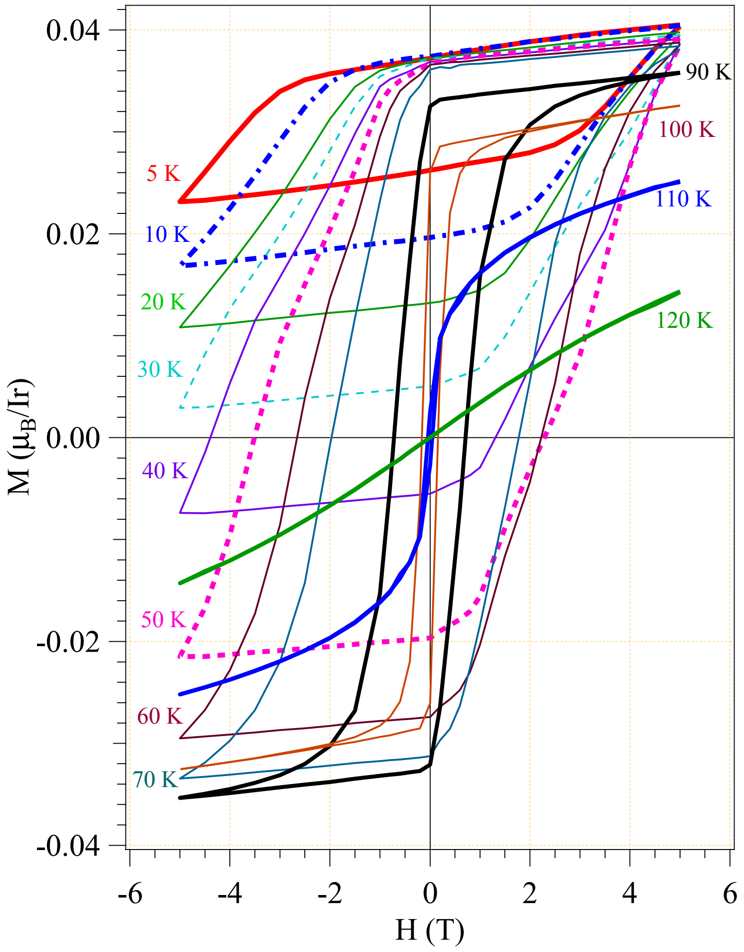

Fig.12 (Color online) The magnetization loop M versus H of the pPv $CaIrO_3$ at different temperatures with zero-field cooling through T_c.

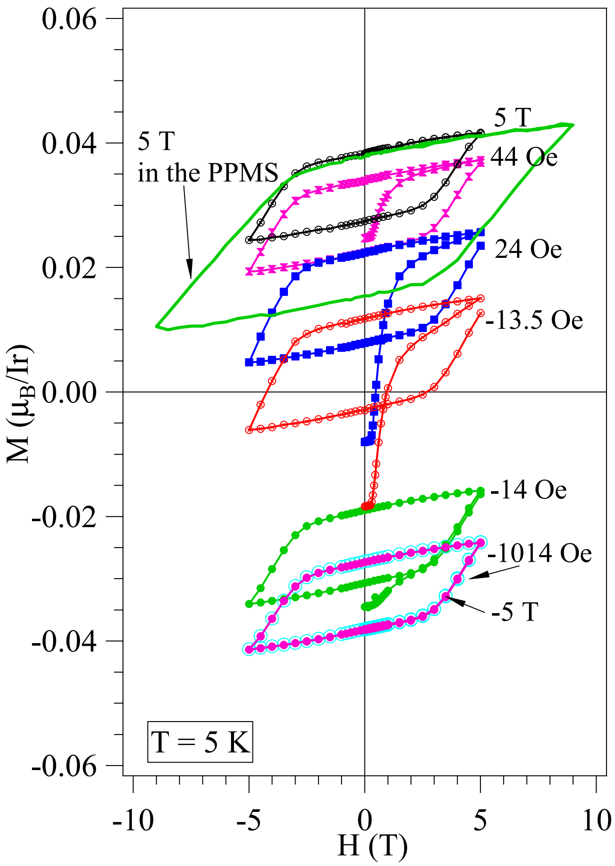

Fig.13 (Color online) The magnetization loop M versus H at 5 K for the pPv $CaIrO_3$ cooled down through T_c under different magnetic fields. Most curves have been obtained with a MPMS except one (± 9 T) with a PPMS.

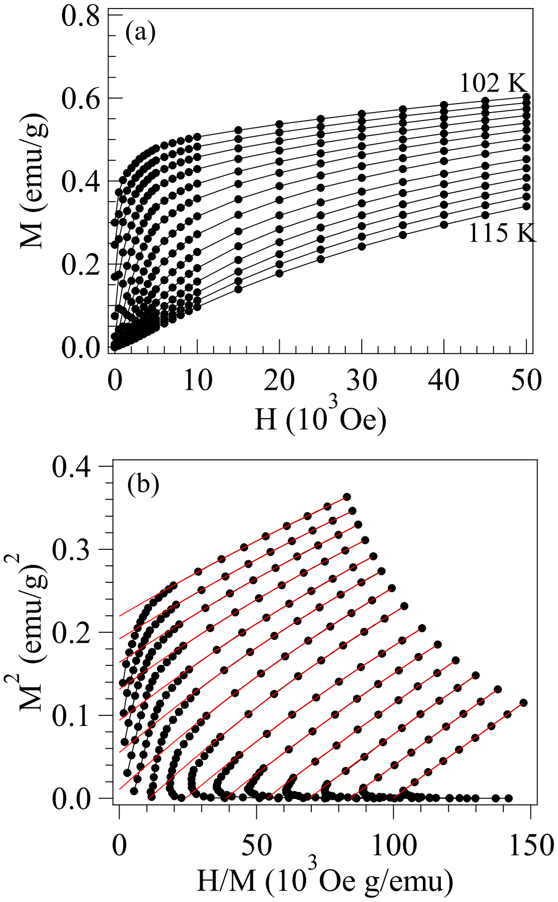

Fig.14 (a) Field dependence of the isothermal magnetization curves M(H) from 102 K to 115 K; (b) the Arrott plot, *i.e.* M^2 vs H/M, of the isotherms and the polynomial fitting curves to the high-field data of the pPv $CaIrO_3$.

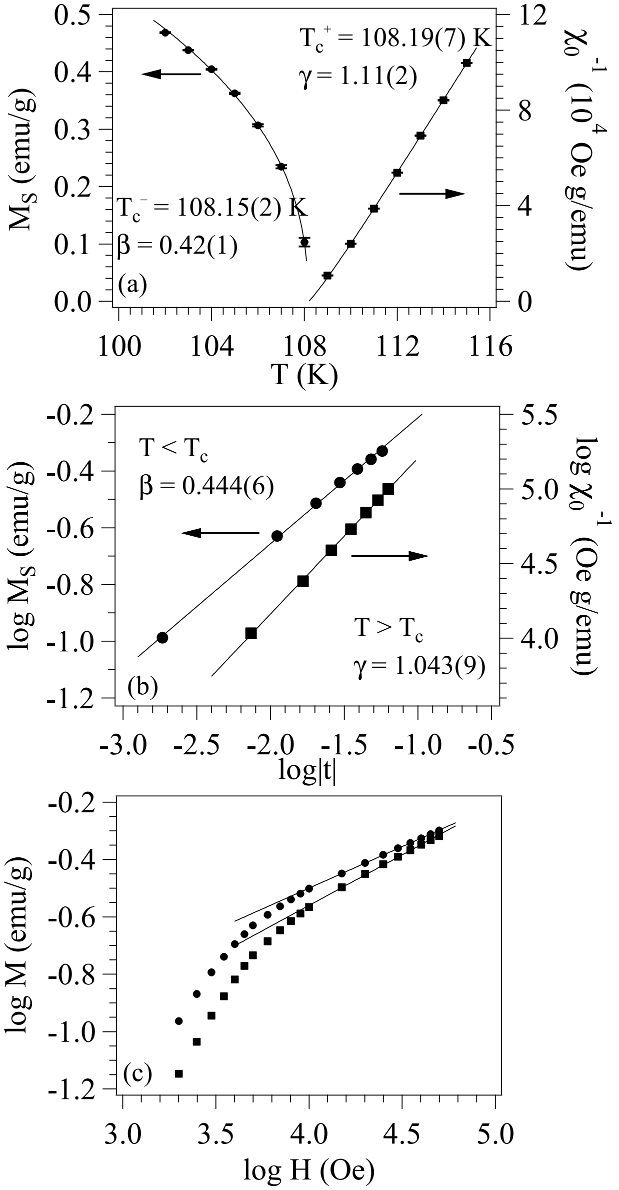

Fig.15 Temperature dependence of the spontaneous magnetization M_s and the inverse initial susceptibility χ_0^{-1} together with the power-law fitting curves; (b) The log-log plots of M_s and χ_0^{-1} versus reduced temperature $|t| \equiv |(T-T_c)/T_c|$ with $T_c = 108.2$ K; (c) The log-log plots of the isotherms at T = 108 K and 109 K of the pPv $CaIrO_3$; an interpolation of these two slopes was used to obtained the slope of the critical isotherm and thus the exponent δ. Other critical exponents have also been given inside the figures.

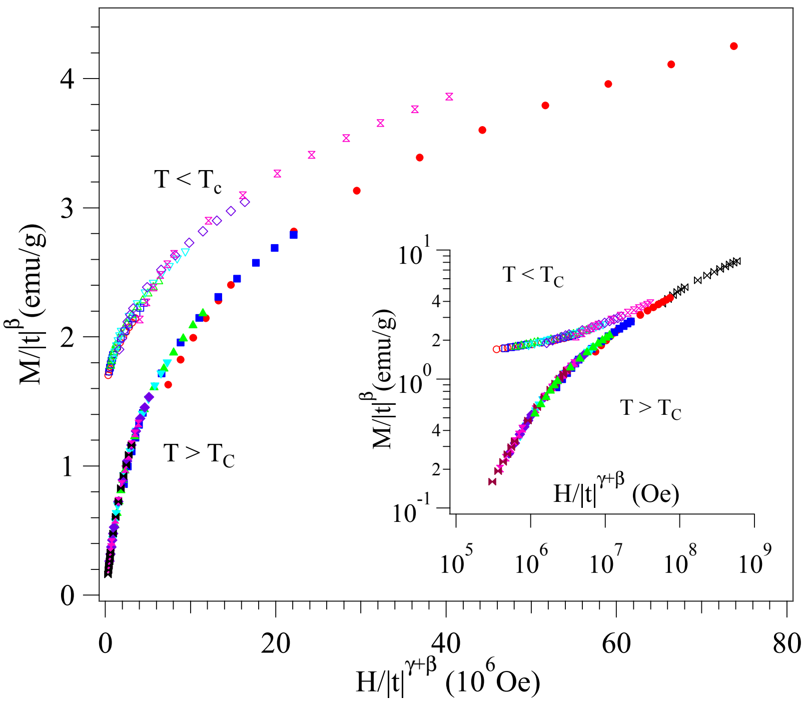

Fig.16 (Color online) A scaling plot of $M/|t|^{\beta}$ vs $H/|t|^{\gamma+\beta}$ below and above T_c with the critical exponents $\beta = 0.444$, $\gamma = 1.043$ and $T_c = 108.2$ K for the pPv $CaIrO_3$. The inset shows the log-log plot of the same data. Isotherms at different temperatures are distinguished by different symbols.

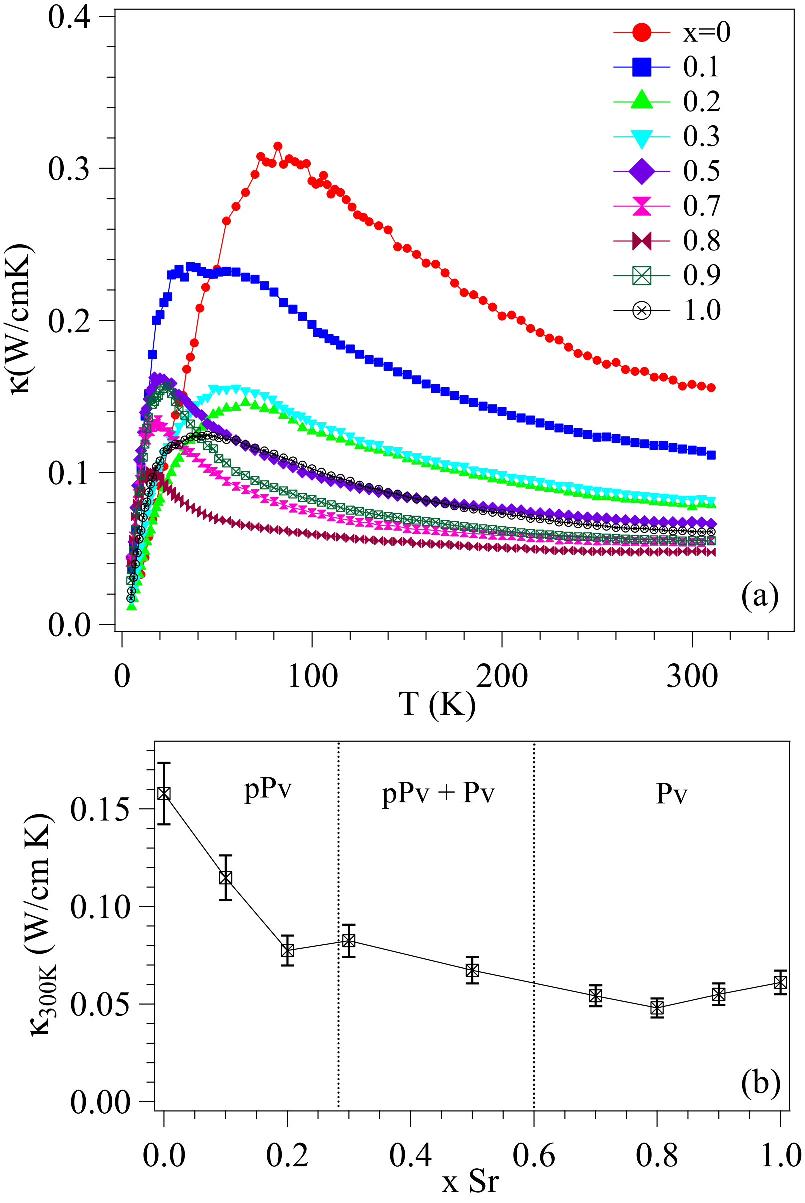

Fig. 17 (Color online) (a) Temperature dependence of thermal conductivity κ and κ(300K) as a function of x in the pPv and the Pv $Ca_{1-x}Sr_xIrO_3$.

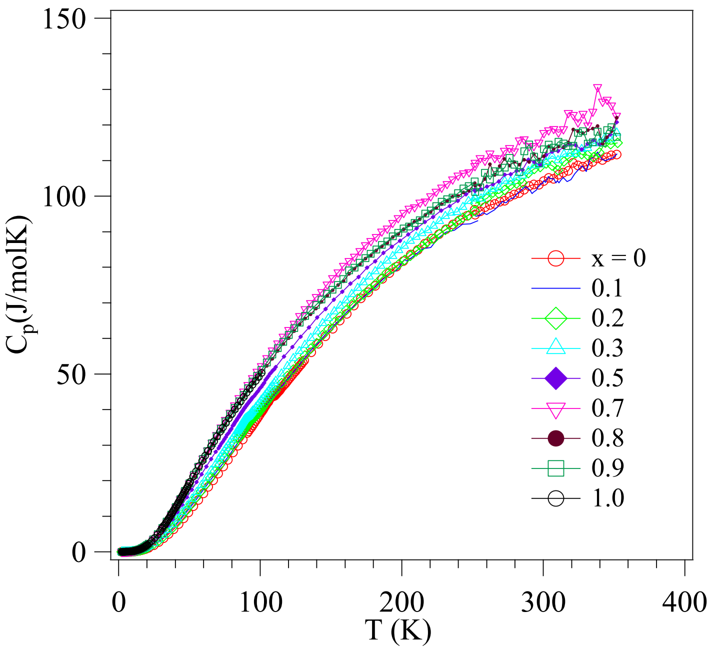

Fig. 18 (Color online) Temperature dependence of specific heat Cp for the pPv and the Pv $Ca_{1-x}Sr_xIrO_3$.

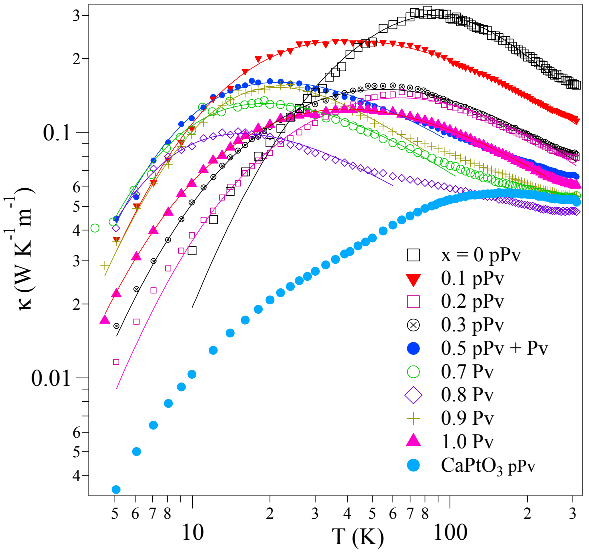

Fig.19 (Color online) Temperature dependence of thermal conductivity κ and curve fitting (solid lines) with the Debye model for the pPv and the Pv $Ca_{1-x}Sr_xIrO_3$ and the pPv $CaPtO_3$.

* jszhou@mail.utexas.edu

---

[1] J.-S. Zhou and J. B. Goodenough, Phys. Rev. Lett. **94**, 065501 (2005).

[2] J.-S. Zhou and J. B. Goodenough, Phys. Rev. B **77**, 132104 (2008).

[3] O. B. Korneta, T. Qi, S. Chikara, S. Parkin, L. E. De Long, P. Schlottmann, and G. Cao, Phys. Rev. B **82**, 115117 (2010).

[4] O. B. Korneta, S. Chikara, S. Parkin, L. E. DeLong, P. Schlottmann, and G. Cao, Phys. Rev. B **81**, 045101 (2010).

[5] S. J. Moon, H. Jin, W. S. Choi, J. S. Lee, S.S. A. Seo, J. Yu, G. Cao, T. W. Noh, and Y. S. Lee, Phys. Rev. B **80** , 195110 (2009).

[6] S. Chikara, O. Korneta, W. P. Crummett, L. E. DeLong, P. Schlottmann, and G. Cao, Phys. Rev. B **80**, 140407 (2009).

[7] S. J. Moon, H. Jin, K. W. Kim, W. S. Choi, Y. S. Lee, J. Yu, G. Cao, A. Sumi, H. Funakubo, C. Bernhard, and T. W. Noh, Phys. Rev. Lett. **101**, 226402 (2008).

[8] G. Cao, V. Durairaj, S. Chikara, L. E. DeLong, S. Parkin, and P. Schlottmann, Phys. Rev. B **76**, 100402 (2007).

[9] G. Cao, V. Durairaj, S. Chikara, S. Parkin, and P. Schlottman, Phys. Rev. B **75**, 134402 (2007).

[10] S. J. Moon, M. W. Kim, K. W. Kim, Y. S. Lee, J.-Y. Kim, J.-H. Park, B. J. Kim, S.-J. Oh, S. Nakatsuji, Y. Maeno, I. Nagai, S. I. Ikeda, G. Cao, and T. W. Noh, Phys. Rev. B **74**, 113104 (2006).

[11] H. Jin, H. Jeong, T. Ozaki, and J. Yu, Phys. Rev. B **80**, 075112 (2009).

---

[12] M. K. Crawford, M. A. Subramanian , R. L. Harlow, J. A. Fernandez-Baca, Z. R. Wang, and D. C. Johnston , Phys. Rev. B **49**, 9198 (1994).

[13] S A. Carter, B. Batlogg, R. J. Cava, J. J. Krajewski, W. F. Peck, Jr., and L. W. Rupp,Jr., Phys. Rev. B **51**, 17184 (1995).

[14] M. A. Laguna-Marco, D. Haskel, N. Souza-Neto, J. C. Lang, V. V. Krishnaumurthy, G. Cao, and M. van Veenendaal, Phys. Rev. Lett. **in press** (2010).

[15] R. D. Cowan, *The Theory of Atomic Structure and Spectra* (Univ. of California Press, Berkeley, 1981), p.238.

[16] B. J. Kim, H. Jin, S. J. Moon, J.-Y. Kim, B.-G. Park, C. S. Leem, J. Yu, T. W. Noh, C. Kim, S.-J. Oh, J.-H. Park, V. Durairaj, G. Cao, and E. Rotenberg, Phys. Rev. Lett. **101**, 076402 (2008).

[17] B. J. Kim, H. Ohsumi, T. Komesu, T. Morita, H. Takagi, and T. Arima, Science **323**, 1329 (2009).

[18] R. S. Perry, F. Baumberger, L. Balicas, N. Kikugawa, N.J.C. Ingle, A. Rost, J. F. Mercure, Y. Maeno, Z.X. Shen, and A.P. Mackenzie, New J. of Phys. **8**, 175 (2006).

[19] G. Jackeli and G. Khaliullin, Phys. Rev. Lett. **102**, 017205 (2009).

[20] M. Murakami, K. Hirose, K. Kawamura, N. Sata, and Y. Ohishi, Science, **304**, 855 (2004); A.R. Oganov and S. Ono, Nature **430**, 445 (2004).

[21] K. Catalli, S.-H. Shim, and V. Prakapenka, Nature **462**, 782 (2009).

[22] T.B. Ballaran, R.G. Tronnes, and D.J. Frost, American Mineralogist **92**, 1760 (2007).

[23] C.D. Martin, K.W. Chapman, P. J. Chupas, V. Prakapenka, P. L. Lee, S. D. Shastri, and J. B. Parise, American Mineralogist **92**, 1048 (2007).

---

[24] L. Miyagi, N. Nishiyama, Y. Wang, A. Kubo, D. V. West, R. J. Cava, T. S. Duffy, and H.-R. Wenk, Earth and Planetary Sci. Lett. **268**, 515 (2008).

[25] N. Miyajima, K. Ohgushi, M. Ichihara, and T. Yagi, Geophys. Res. Lett. **33**, L12302 (2006).

[26] C. D. Martin, J. Appl. Crystallo. **41**, 776 (2008).

[27] J. Hustoft, S.-H. Shim, A. Kubo, and N. Nishiyama, American Mineralogist **93**, 1654 (2008).

[28] C D. Martin, R. I. Smith, W. G. Marshall, and J. B. Parise, American Mineralogist **92**, 1912 (2007).

[29] H. Kojitani, Y. Shirako, and M. Akaogi, Physics of the Earth and Planetary Interiors **165**, 127 (2007).

[30] Y. Shirako, H. Kojitani, M. Akaogi, K. Yamaura, and E. Takayama-Muromachi, Phys. Chem. Minerals **36**, 455 (2009).

[31] K. Yamaura, Y. Shirako, H. Kojitani, M. Arai, D. P. Young, M. Akaogi, M. Nakashima, T. Katsumata, Y. Inaguma, and E. Takayama-Muromachi, J. Am. Chem. Soc. **131**, 2722 (2009).

[32] Y. Inaguma, K. Hasumi, M. Yoshida, T. Ohba, and T. Katsumata, Inorg. Chem. **47**, 1868 (2008).

[33] K. Ohgushi, Y. Matsushita, N. Miyajima, Y. Katsuya, M. Tanaka, F. Izumi, H. Gotou, Y. Ueda, and T. Yagi, Phys. Chem. Minerals **35**, 189 (2008).

[34] K. Ohgushi, H. Gotou, T. Yagi, Y. Kiuchi, F. Sakai, and Y. Ueda, Phys. Rev. B **74**, 241104 (R) (2006).

---

[35] K. Ohgushi, Koatsuryoku no kagaku to gijutsu **18**, 237 (2008).

[36] K. Ohgushi, T. Yagi, H. Gotou, Y. Kiuchi, and Y. Ueda, Physica B **404**, 3261 (2009).

[37] J. G. Cheng, J. A. Alonso, E. Suard, J. S. Zhou, and J. B. Goodenough, J. Am. Chem. Soc. **131**, 7461 (2009).

[38] R. F. Sarkozy, C. W. Moeller, and B. L. Chamberland, J. Solid State Chem. **9**, 242 (1974).

[39] J. Wang, B. H., Toby, P. L. Lee, L. Ribaud, S. Antao, C. Kurtz, M. Ramanathan, Von R. B. Dreele, and M. A. Beno, Rev. Sci. Instru. **79**, 085105 (2008).

[40] J. Rodríguez-Carvajal, Physica B **192**, 55 (1993).

[41] C. L. McDaniel and S. J. Schneider, J. Solid State Chem. **4**, 275 (1972).

[42] K. Niwa, T. Yagi, and K. Ohgushi, Phys. Chem. Mineral. **in press** (2010).

[43] M. Sugahara, A. Yoshiasa, A. Yoneda, T. Hashimoto, S. Sakai, M. Okube, A. Nakatsuka, and O. Ohtaka, Am. Mineral. **93**, 1148 (2008).

[44] J. B. Goodenough, Phys. Rev. **171**, 466 (1968).

[45] O. Chmaissem, B. Dabrowski, S. Kolesnik, J. Mais, D. E. Brown, R. Kruk, P. Prior, B. Pyles, and J. D. Jorgensen, Phys. Rev. B **64**, 134412 (2001).

[46] G. Cao, S. McCall, M. Shepard, J. E. Crow, and P. P. Guertin, Phys. Rev. B **56**, 321 (1997).

[47] M. Akaogi, private commu.

[48] K. Yamaura and E. Takayyama-Muromachi, Physica C **445**, 54 (2006).

[49] I. H. Inoue, O. Goto, H. Makino, N. E. Hussey, and M. Ishikawa, Phys. Rev. B **58**, 4372 (1998).

---

[50] M. Cyrot, B. Lambert-Andron, J. L. Soubeyroux, M. J. Rey, Ph. Dehauht, F. Cyrot-Lackmann, G. Fourcaudot, J. Beille, and J. L. Tholence, J. Solid State Chem. **85**, 321 (1990).

[51] S. Nakatsuji and Y. Maeno, Phys. Rev. Lett. **84**, 2666 (2000).

[52] N. S. Kini, A. M. Strydom, H. S. Jeevan, C. Geibel, and S. Ramakrishnan, J. Phys.: Condens Matter **18**, 8205 (2006).

[53] D. K.C. MacDonald, *Thermoelectricity: An Introduction to the Principles* (Wiley, New York, 1962)

[54] J.-S. Zhou and J. B. Goodenough, Phys. Rev. B **51**, 3104 (1995).

[55] J.-S. Zhou and J. B. Goodenough, Phys. Rev. B **68**, 054403 (2003).

[56] J. B. Goodenough and J.-S. Zhou, in *Localized to Itinerant Electronic Transition in Perovskite Oxides, Structure & Bonding*, edited by J. B. Goodenough (Springer, Berlin, 2001), Vol. **98**, p.17.

[57] J.-S. Zhou, J. B. Goodenough, J.-Q. Yan, and Y. Ren, Phys. Rev. Lett. **99**, 156401 (2007).

[58] J. Stohr and H. C. Siegmann, *Magnetism* , (Springer-Verlag, Berlin, 2006), p.619.

[59] H. E. Stanley, *Introduction to Phase Transitions and Critical Phenomena* (Oxford University Press, London, 1971)

[60] A. Arrott, Phys. Rev. **108**, 1394 (1957).

[61] B. Widom, J. Chem. Phys. **41**, 1633 (1964); **43**, 3898 (1965).

[62] E. C. Stoner, Proc. R. Soc. London, Ser. A **165**, 372 (1938).

[63] E. P. Wohlfarth, J. Appl. Phys. **39**, 1061 (1968).

---

[64] H. E. Stanley, *Introduction to Phase Transitions and Crtical Phenomena* (Oxford University Press, London, 1971)

[65] E. A. Yelland, S. J. C. Yates, O. Taylor, A. Griffiths, S. M. Hayden, and A. Carrington, Phys. Rev. B **72**, 184436 (2005).

[66] A. Arrott and J. E. Noakes, Phys. Rev. Lett. **19**, 786 (1967).

[67] F. Y. Yang, C. L. Chien, X. W. Li, G. Xiao, and A. Gupta, Phys. Rev. B **63**, 092403 (2001).

[68] H. Yanagihara, W. Cheong, M. B. Salamon, Sh. Xu, and Y. Moritomo, Phys. Rev. B **65**, 092411 (2002).

[69] K. Ghosh, C. J. Lobb, R. L. Greene, S. G. Karabashev, D. A. Shulyatev, A. A. Arsenov, and Y. Mukovskii, Phys. Rev. Lett. **81**, 4740 (1998).

[70] W. Jiang, X. Z. Zhou, Gwyn Williams, Y. Mukovskii, and K. Glazyrin, Phys. Rev. B. **78**, 144409 (2008).

[71] X. Luo, Y. P. Sun, X. B. Zhu, and W. H. Song, J. Phys.: Condens. Matter **20**, 465211 (2008).

[72] J.-G. Cheng, Y. Sui, J.-S. Zhou, J. B. Goodenough, and W. H. Su, Phys. Rev. Lett. **101**, 087205 (2008).

[73] T. Kida, A. Senda, S. Yoshi, M. Hagiwara, T. Takeuchi, T. Nakano, and I. Terasaki, Europhys. Lett. **84**, 27004 (2008).

[74] J.-G. Cheng, J.-S. Zhou, J. A. Alonso, J, B. Goodenough, Y. Sui, K. Matsubayashi, and Y. Uwatoko, Phys. Rev. B **80**, 104430 (2009).

[75] S. N. Kaul, J. Mag. and Mag. Mater. **53**, 5 (1985).

---

[76] K. Hirose, Scientific American **302**, 76 (2010).

[77] R. Berman, *Thermal Conduction in Solids* (Clarendon Press, Oxford, 1976).

[78] J.-G. Cheng, J.-S. Zhou, and J. B. Goodenough, Phys. Rev. B **79**, 184414 (2009).

[79] J.-Q. Yan, J.-S. Zhou, and J. B. Goodenough, Phys. Rev. Lett. **93**, 235901 (2004).

[80] M. K. Crawford, M. A. Subramanian, R. L. Harlow, J. A. Fernandez-Baca, Z. R. Wang, and D. C. Johnston, Phys. Rev. B **49**, 9198 (1994).